High temperature vat photopolymerization 3D printing of fully bio-based composites: Green vegetable oil epoxy matrix & bio-derived filler powder

Additive Manufacturing 79 (2024) 103929

Contents lists available at ScienceDirect

Additive Manufacturing

journal homepage: www.elsevier.com/locate/addma

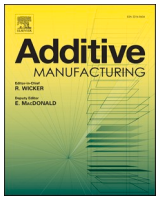

High temperature vat photopolymerization 3D printing of fully bio-based composites: Green vegetable oil epoxy matrix & bio-derived filler powder

Lorenzo Pezzana [a], Raffael Wolff [b], Jürgen Stampfl [c], Robert Liska [b], Marco Sangermano [a,*]

[a] Dipartimento Scienza Applicata e Tecnologia, Politecnico di Torino, Corso Duca degli Abruzzi 24, 10129 Torino, Italy
[b] Institute of Applied Synthetic Chemistry, Technische Universität Wien, Getreidemarkt 9/163 MC, 1060 Vienna, Austria
[c] Institute of Material Sciences and Testing, Technische Universität Wien, Getreidemarkt 9/E308, 1060 Vienna, Austria

ARTICLE INFO

Keywords:
VAT photopolymerization
Bio-based monomers
UV-Curing
Epoxy
Bio-composites

ABSTRACT

Additive manufacturing (AM) is a well-established process which allows to generate complex and accurate geometry required in several applications, from medical to automotive area. The exploitation of polymer resin into additive manufacturing needs to overcome the problem of viscosity and reactivity which can be improved by high temperature vat photopolymerization (VPP). Moreover, the concern about climate change and depletion of fossil fuels arises the requirement to move toward bio-derived products which can substitute the commercially available resins without compromise the final properties. In order to close this gap, we have studied vegetable epoxy oil polymer resins as main component for new bio-derived formulations which can be used in vat photopolymerization 3D printing. Furthermore, knowing the limits of the vegetable oils in terms of final properties, the investigation explores the possibility to 3D printing bio-derived composites by adding bio-based fillers, such as wall-nut shell. The UV-curing process was investigated by photo-DSC and photorheology to verify the feasibility of AM. Then, the effect of the presence of the filler on the UV-process was assessed and finally we successfully 3D printed composites of different geometries. The thermo-mechanical properties of the thermoset materials were studied by dynamic analysis and tensile testing. The benefit of the addition of the filler was confirmed and explained by investigating the surface modification of the filler which had an incredible impact on the properties of the composite. Finally, we pursuit the possibility to chemically degrade the thermoset joining the proof-of-concept of circular economy.

1. Introduction

Additive manufacturing has experienced widespread popularity and implementation over the past decade as a technology for material production, both in academia and industry [1,2]. Several applications can be covered spanning from biomedical [3,4], to electronics [5,6], and aerospace components [7,8]. This technology allows for the creation of complex 3D structures, significantly reducing production time and cost [9,10]. Among the different 3D printing techniques for polymers, light-induced processes such as stereolithography (SLA) and digital light processing (DLP) are gaining increasing importance [11]. These processes offer high spatial resolution and superior accuracy compared to other methods [2].

A recent advancement in light-induced technology is the introduction of a heated printing chamber called Hot Lithography which enable the performance of printing job at elevated temperatures (i.e. over 100 °C) [12,13]. Originally designed for processing high-viscosity resins, this approach yields to a reduction in the viscosity and subsequently an easy processability of the polymeric precursors. Additionally, it has been demonstrated that UV-curing mechanisms exhibit significantly accelerated curing kinetics at higher temperatures, leading to a higher degree of conversion [14].

Consequently, this breakthrough allows the processing of new types of resins, such as oxazolines [15], cyclic polyesters [16] or epoxy resins [17], which are not reactive enough at room temperature to be exploited in 3D printing technology. This expansion in formulation design and selection opens up new possibilities in additive manufacturing. Indeed, in previous studies, we investigated the feasibility of SLA Hot Lithography employing a fossil-based, commercially available epoxy resin bisphenol A diglycidyl ether (BADGE) [17]. The success in the printing opened the portfolio to new resins which cannot be employed at room temperature due to high viscosity or slow kinetics.

* Correspondsing author.
E-mail address: marco.sangermano@polito.it (M. Sangermano).

https://doi.org/10.1016/j.addma.2023.103929
Received 28 September 2023; Received in revised form 13 December 2023; Accepted 15 December 2023
Available online 22 December 2023

The growing concerns surrounding climate change and the depletion of fossil fuel resources have sparked increased efforts to develop new biobased chemicals as alternatives to petroleum-derived products. [18,19] By utilizing low-cost renewable feedstocks like food and forestry wide stream, researchers aim to establish a sustainable approach for producing innovative derivatives [20–22]. Biomass resources such as lignin, cellulose, and hemicellulose offer a promising starting point, as they can be converted into platform chemicals or building blocks such as terpenes [23,24], furan derivatives [25–27], phenols [20,28], and isosorbide [29–32]. Furthermore, different biomass, such as seed, nuts, or fruit of various plant are promising resources for vegetable oils which can be used for several applications [33–35].

In our previous paper we have investigated the use of bio-based epoxy resins in Hot Lithography comparing the properties of the derived thermoset with a fossil-based diglycidyl ether [36]. This study allowed to confirm the possibility to use bio-based resin instead of fossil ones obtaining similar properties.

The use of vegetable oils as a renewable resource for producing epoxidized derivatives offers advantages such as their abundance, low cost, and potential biodegradability [37,38]. They are composed of triglycerides with a high content of double bonds which can be converted into epoxy functional group with yield over 90% [39,40]. Several studies reported the use of methacrylated or acrylated derivatives from vegetable oils which can be used for 3D printing. Both DLP [41,42] and SLA [43] were employed to achieve new bio-derived inks. Acrylated soybean oil was exploited in a 3D printing process in presence of ultra-low content of cellulose [44] and modified cellulose [45] or macadamia nutshell [46] which were used as reinforcing agents to tailor and modify the final properties of the thermoset. The introduction of nanocellulose in acrylated vegetable oil resins provided an increase up to a 2.5-fold in strength and 4-fold in toughness reached by surface functionalization of the filler to increase the compatibility between polymer matrix and filler [47]. Furthermore, cellulose nanofibers were employed to reinforce a medical-grade acrylate resin reaching massively increment of strength [48]. Sunflower fatty acid and modified nanocellulose were proposed as 3D printable formulation to develop green composite with enhanced mechanical properties, the functionalization aimed to increase the compatibility decreasing the agglomeration [49].

Driven by the concerning about circular economy and sustainable materials, we further developed this additive manufacturing portfolio investigating the possibility to develop polymer composites in the field of epoxy-based resins which are less investigated than acrylated ones. We investigate the use of non-edible epoxy oils in Hot Lithography as polymer matrix with bio-derived powder fillers such as walnut shell, hemp and tagua.

For the best of our knowledge, there are no studies about the Hot Lithography of fully bio-based composite originated from epoxy vegetable oils (EVOs). Thus, we investigate the use of epoxy linseed oil (ELO) and epoxy soybean oil (ESO) as matrix for bio composite. We employed bio-derived fillers such as walnut shell (WS), tagua (T), and hemp (H) to arise the total bio-content in the different composites. We studied the UV-curing process to understand the feasibility of the additive manufacturing and we asset the thermo-mechanical properties of the composite by DMA analysis. We further investigated the tensile properties of the composite, and the possible interaction between matrix and filler to understand the benefit of the filler. Finally, we studied the potential degradation of the composite and the recyclability of the polymer matrix.

2. Materials and methods

2.1. Materials

The epoxy linseed oil (**ELO**) and the epoxy soybean oil (**ESO**) were gently given from HOBUM Oleochemicals GmbH (Hamburg, Germany). According to the specification given by the company, ELO had an acid value $\leq$ 1.0 mg KOH/g, while ESO had a value $\leq$ 0.5 mg KOH/g; the iodine values were $\leq$ 7.0 g and $\leq$ 3.5 g I_2/100 g for ELO and ESO respectively. The viscosity of ELO measured at 25 °C varied from 800 to 1300 mPa×s while ESO had a value between 400 and 600 mPa×s. The bio-based fillers were donated from Composition Materials Co., Inc. (Milford, USA). Wall-nut shell powder (WS) was provided in two different mesh, 200 and 325, labelled **WS200** and **WS325** respectively. Furthermore, tagua powder (**T200**) and hemp powder (**H200**) with a 200 mesh were provided. According to the standard sieve specification used by the company, the mesh 200 indicate a minimum of 88% of particles below 75 μm while the mesh 325 ensure that at least 88% of particle have a diameter below 45 μm. The photoinitiator, p-(octyloxyphenyl)phenyl iodonium hexafluoroantimonate, (**I-SbF6**), 95%, was purchased from ABCR. The sensitizer isopropylthioxanthone (**ITX**) was supplied from Lambson. The triarylsulfonium hexafluoroantimonate (**S-SbF6**) salts mixed to 50 wt% in propylene carbonate were purchased from Sigma Aldrich. Tris(4-((4-acetylphenyl)thio)phenyl) sulfonium tetrakis(pentafluorophenyl) borate (**S-BF5**) 95%, Irgacure 290, was supplied by BASF. The trimethylchlorosilane (**$Si(CH_3)_3Cl$**) was purchased from VWR Chemicals. Triethylamine (**TEA**) was purchased from Sigma Aldrich. Dichloromethane (**DCM**) was provided by VWR Chemicals. Deuterated chloroform $CDCl_3$, and dimethyl sulfoxide, DSMO-d_6, were purchased from Sigma Aldrich and used as solvent and reference for NMR analyses.

2.2. Formulations and hot stereolithography SLA 3D prinitng

The epoxy vegetable oils were added with 3 phr (per hundred resin) of the three selected photoinitiators in order to test the reactivity and the thermal stability. The selected photoinitiators were S-SbF6, I-SbF6 used with ITX as sensitizer, and S-BF5 respectively. Once we established the best formulation, we adopted the selected photoinitiator for the further investigations. The photoinitiator was mixed in 3 phr with respect to the resin and mixed in ultrasound bath until the complete dissolution of the photoinitiator (30 min). The filler was added with respect to the resin weight (i.e. 5, 10 or 20 phr) in a second step according to Table 1. The formulations were repeated for epoxy soybean oil (ESO) adding the same amount of filler as the formulations containing ELO. Mechanical mixing was provided to the formulations to homogenize and distribute the filler by Vortex Genie for 5 min at 300 rpm. The formulations were handled in brownish vials to avoid light contact and the components were weighted in an orange room.

Table 1
Formulations studied with epoxy linseed oil (ELO) and soybean oil (ESO) and the different fillers, wall-nut shell (WS200 and WS325), tagua (T200), and hemp (H200) powder. The photoinitiator used was S-BF5 in 3 phr with respect to the epoxy resin, while the filler varied in the distinct formulations according to the table: [XX] indicate the filler's phr used in each formulation.

ENTRY	*VEGETABLE EPOXY OIL*	*FILLER [phr]*
ELO	ELO	/
ELO_WS325_10	ELO	WS325[10]
ELO_WS325_20	ELO	WS325[20]
ELO_WS200_10	ELO	WS200[10]
ELO_WS200_20	ELO	WS200[20]
ELO_T200_10	ELO	T200[10]
ELO_T200_20	ELO	T200[20]
ELO_H200_5	ELO	H200[5]
ELO_H200_10	ELO	H200[10]
ESO	ESO	/
ESO_WS325_10	ESO	WS325[10]
ESO_WS325_20	ESO	WS325[20]
ESO_WS200_10	ESO	WS200[10]
ESO_WS200_20	ESO	WS200[20]
ESO_T200_10	ESO	T200[10]
ESO_T200_20	ESO	T200[20]
ESO_H200_5	ESO	H200[5]
ESO_H200_10	ESO	H200[10]

The formulations were tested and used for the 3D printing, around 15 g batch were prepared each time to fulfill the printing. The SLA 3D printer used in this work was a Caligma 200 UV prototype developed by Cubicure (Vienna, Austria) with a bottom exposure SLA setup. The different components of the printer, specifically the vat, the building platform, and the coating unit were heated up to 100 °C. The laser emission was centered at the wavelength of 375 nm with power of 70 mW/mm^2, while the laser spot diameter was set at 25 μm during printing. The laser beam is scanned over a 2-dimensional plane using a galvanometer scanning system; the layer thickness of the resin was kept at 100 μm for all the printing job. The speed was adjusted according to the formulation used varying from 1000 to 500 mm/s for pristine formulations and filled one respectively. The different geometries were developed through a CAD file saved in extension.cli to be read by the printer software.

2.3. Silanization of wall-nut shell

The silanization reaction was performed according to previous protocol reported in literature [50,51]. The WS325 (5 g) was suspended in anhydrous DCM in a three-bottom round flask. $Si(CH_3)_3Cl$ was added in ratio 1:10 (50 g) to ensure the excess of the silane reagent. TEA (1.2 equivalent of $Si(CH_3)_3Cl$) was mixed with 20 mL of DCM and was added drop wise through adding funnel. The reaction was kept under nitrogen atmosphere at room temperature with high mixing guarantee by magnetic stirring. The reaction last for 24 h then the reaction was stopped by neutralization adding saturated solution of $NaHCO_3$. This step was done in an ice bath to keep control over the temperature due to the exothermicity of the reaction step. The final suspension was filtered through a Buchner funnel (porosity 4) and rinsed with deionized water multiple times to eliminate the possible formation of salt. WS325_SIL was then recovered and dried in a vacuum oven over night at 50 °C.

2.4. Characterization

2.4.1. Nuclear magnetic resonance (NMR)

^{1}H NMR spectra of the pristine resins, ELO and ESO were recorded on a Bruker Avance at 400 MHz; chemical shifts are given in ppm and were referenced to the solvent residual peak ($CDCl_3$). The degraded product was dissolved in DMSO-d_6 and ^{1}H NMR spectra was registered and referred to the solvent residual peak.

2.4.2. Epoxy number

Epoxy number was evaluated with titration to corroborate the NMR data (Fig. S1). The standard procedure was used. [52] Briefly, 1 g of resin was reacted with 50 mL of pyridinium hydrochlorine solution for 20 min under reflux. After cooling down to room temperature, the residual HCl was titrated against NaOH 0.1 N using an automated titration device Methrom 848 titrino plus. Triplicates of resin and blind resins were done. The epoxy value (mol/kg) was calculated according to Eq. (1).

$$Epoxy \quad value = f \times N \times \frac{B - A}{m} \tag{1}$$

Where f is the correction factor of aqueous NaOH; N is normality of NaOH (mmol/mL); B is volume of NaOH used for blind solution (mL); A is the volume of NaOH used for sample titration (mL); m is the mass of resin sample (g).

2.4.3. Photo-differential scanning calorimetry (PHOTO-DSC)

Photo-DSC measurements were conducted on a Netzsch DSC 204 F1 with autosampler. All tests were performed in isothermal condition at different temperatures, at 25, 50, 75, and 100 °C under a N2 atmosphere. The resins (10–15 mg) were irradiated twice with filtered UV-light (320 −500 nm) via an Exfo OmniCureTM series 2000 broadband Hg lamp under constant N_2 flow (20 mL/min). The light intensity was set around to 60 mW/cm^2 on the surface of the sample. The heat flow of the polymerization reaction was recorded as a function of time. The first curve derived from the first irradiation was subtracted to the one derived from the second to correct the measure. The important parameters detected through this analysis were: the time of which the maximum of heat evolution was reached (t_{max}), the height of the exothermic peaks (h_{peak}), and the total enthalpy (ΔH), evaluated as the integration of the curing peak. All measurements were performed in triplicate with satisfactory reproducibility. The epoxy conversion (EC_{DSC}) was evaluated according to Eq. (2).

$$EC_{DSC} = \left(\frac{\Delta H \times f_f}{Epoxy \quad value}\right) \times \Delta H_0^{-1} \tag{2}$$

Where ΔH_0 is the total enthalpy generated from the cross-linking reaction (J/g); f_f is the correction factor used for the formulation containing the filler; *Epoxy value* is the epoxy value of the resin used for the different formulations (mol/kg); ΔH is the theoretical enthalpy which was between 66 and 75 kJ/mol [53,54].

The photo-DSC also allowed the evaluation of the Rate of Polymerization (R_P) by Eq. (3).

$$R_P = \frac{h_{peak} \times \rho \times 1000}{\Delta H_0} \tag{3}$$

Where h_{peak} is the height of the photo-DSC exothermic reaction peak (W/g); ρ is the density (g/mL) of the resin evaluated by pycnometer (triplicates were measured to determine the value); ΔH_0 is the theoretical enthalpy (kJ/mol).

2.4.4. Attenuated total reflectance-fourier transform infrared spettroscopy (ATR-FTIR)

The ATR-FTIR spectra were recorded on a Perkin Elmer Spectrum 65 equipped with diamond crystal. The spectra were collected in a range between 4000–500 cm^{-1} and 32 scans with resolution of 4 cm^{-1} were performed for each sample. For the analysis of the results, the software Spectrum from Perkin Elmer in version 10.03.07.0112 was used. Liquid formulations before UV-irradiation, cross-linked network after UV-irradiation, filler powders, functionalized filler and degraded product were tested. The epoxy peak taken in consideration was located at 825 cm^{-1}. The spectra were normalized by the ester peak at 1738 cm^{-1} which was assumed to be unaffected by the cationic UV-curing. The epoxy conversion (EC_{FTIR}) was evaluated according to Eq. (4).

$$EC_{FTIR} = \left(1 - \frac{A_{@T}}{A_i}\right) \times 100 \tag{4}$$

Where $A_{@T}$ is the epoxy area after the UV-curing at certain temperature; A_i is the initial epoxy area before the UV-irradiation. The spectra were normalized by the ester peak located at 1738 cm^{-1}.

2.4.5. Photorheology

An Anton Paar MCR302 WESP rheometer was used for photorheology studies. The bottom plate of the rheometer was a borosilicate disk to guarantee the irradiation of the sample. The source for initiating photopolymerization reactions, was UV-light projected via a waveguide on the surface of the sample through the bottom window using an Exfo OmniCure 2000 light source with a broadband Hg-lamp (320–500 nm). The intensity was set around 60 mW/cm^2 at the contact with the sample. The calibration was done by means of Ocean Optics USB 2000 +spectrometer. The rheometer was set as plate-plate geometry with a steel accessory with diameter of 25 mm (PP25). The thickness of the layer was set as 200 μm and 150 μL of resin was dropped in the center of the bottom glass plate. The tests were performed at different temperature: 25, 50, 75 and 100 °C. The temperature can be controlled by Peltier elements located around the window holder in the

temperature control system (Anton Paar P-PTD200/GL). Additional heating from above by an external Peltier-controlled hood was employed for experiments at elevated temperatures (H-PTD 200 from Anton Paar). The measurements were performed in triplicate to have reproducible data. RheoCompass 1.24 was used to analyze the results.

2.4.6. Simultaneous thermogravimetry–differential scanning calorimetry (STA)

The resins were tested by means of STA 449F1 Jupiter from Netzsch in order to evaluate the curing stage and the start of the degradation. Uncured formulations of ELO and ESO were tested to investigate the thermal stability and the thermal activation of the photoinitiators employed. Moreover UV-cured samples were analyzed to investigate the possibility of post curing. The samples around 15 mg were placed into aluminum pan and sealed. The test was performed in controlled atmosphere of N_2 with 20 mL/min flow. The temperature ramp was set with an increase of 10 °C/min from room temperature (r.t.) to 300 °C; after the samples were cooled down to r.t. with 20 °C/min. The data of weight loss and heat flow were analyzed by NETZSCH-Proteus-80. T_{95} was evaluated as the temperature which the sample had 5% of weight loss.

2.4.7. Stability test

The stability test was performed to evaluate the stability of the different formulation at the printing temperature. An Anton Paar MCR300 was used to examine the viscosity of the formulations through the time. A plate-plate geometry was chosen, and the diameter of the support was 25 mm. The distance between the disks used to perform the analyses was 400 μm. The formulations were kept at printing temperature for all the time in an oven. The viscosity was measured by applying an increase shear stress from 1 to 100 1/s after 60 s of stabilization.

2.4.8. Dynamic mechanical thermal analysis (DMTA)

Dynamic Mechanical Thermal Analysis (DMTA) was performed using an Anton Paar MCR 301 device with a CTD 450 oven and an SRF 12 measuring system. The 3D printed DMTA samples at 100 °C were tested in torsion mode with a frequency of 1 Hz and a strain of 0.1%. The dimensions were 40 mm × 4 mm x 2 mm. The temperature was increased from − 50 to 150 °C with a heating rate of 2 °C/min. The glass transition temperature was defined as the temperature at the maximum loss factor (*Tan δ*). The cross-link density was evaluated according to Eq. (5).

$$\upsilon = \frac{E'}{3RT} \tag{5}$$

Where E' is the storage modulus in the rubbery plateau region at T_g + 50 °C, R is the gas constant, and T is the absolute temperature in K.

2.4.9. Tensile test

The tensile test of the printed dog bone samples was performed by means of Zwick Z050 equipped with a 1 kN load cell (Zwick Roell, Ulm, Germany) according to ISO 527 with a test speed of 5 mm/min. The shape of the specimens was a type 5B and five samples for each formulation were tested. The printing was done at the same temperature and same layer thickness. The stress-strain curves were recorded and analyzed via testXpert II testing software. The Young's modulus I (E) was evaluated in the linear portion of the stress-strain curve from the start of the test. The strength at break (σ) was evaluated as the maximum of the stress-strain curve while the elongation at break (ε) was assessed at the rupture of the sample. The toughness (U) was calculated as the area under the stress-strain curve.

2.4.10. Gel content

The % gel analysis was performed by evaluation of weight loss after the immersion of 3D printed sample (150–200 mg) in chloroform for 24 h at room temperature. After the immersion the sample were dried over night at room temperature with a final stage of 1 h at 50 °C to ensure the removal of the residual solvent. The Eq. (6) was used for the calculation of the insoluble fraction. Triplicates were done for each composite tested.

$$\%gel = \frac{W_1}{W_0} * 100 \tag{6}$$

Where W_1 is the weight after the immersion in the solvent; W_0 is the initial weight of the sample.

2.4.11. Morphological analysis: optical miscroscopy, scanning electron microscopy (SEM)

The morphological and surface analysis of the 3D printed samples was carried out using an optic microscope Leica Z16 APO A with a photo camera Leica MC 170 HD to acquire the images. Magnification of 5 ×, 10 ×, and 20 × was used to investigate the surface of the 3D printed objects. The scanning electron microscopy analysis was instead used to investigate the morphology of the filler and the fracture of the tensile samples after the tensile test. A FESEM, Zeiss SUPRA 40 was used in a 75% InLens and 25% secondary mode to obtain the best resolution. The fillers and the tensile samples were glue on SEM stub by carbon tape and metal clamps, then a coating of 5 nm of Pt was spread on top of the sample to ensure conductivity all through the sample.

2.4.12. 3D scanning analysis

The 3D printed square nets were scanned with a 3Shape E3 scanner to verify the precision and accuracy of the printing. The sample were coated with magnesium stearate in order to limit the reflection of light on the structure, and then positioned on a platform by means of a sticky paste to ensure the correct acquisition of images. The resulting scanned images were then compared to the original CAD model by means of CA Analyzer software to generate the deviation analysis and overlay map.

2.4.13. Chemical degradation

The 3D printed samples derived from tensile test (100–150 mg) were immersed into an alkaline solution of NaOH 10 M (20 mL) and magnetically stirred (300 rpm) on a thermoregulate mixer at 80 °C. The samples were recovered from the solution, washed with acidic solution to avoid salt formation and deionized water, then they were dried overnight in a vacuum oven at 60 °C and weighted. The loss evaluation over time was performed according to the Eq. (7) was used for the evaluation.

$$Mass \quad fraction(\%) = \frac{W_r}{W_i} \times 100 \tag{7}$$

where W_r is the weight of the residual sample after the treatment in NaOH and W_i is the initial weight of the sample before the treatment.

The mixtures derived from ELO and ELO_T200_20 after the treatment were centrifugate by means of Centrifuge 5804 R, Eppendorf. The yellow solution was acidified with HCl, and the final precipitate was centrifugate. ATR-FTIR analysis and ^{1}H NMR analysis were carried out on the final product.

3. Result and discussion

3.1. Selection of photoinitiator system for Hot Lithography

The selection of the photoinitiator system is tremendously important due to the implication about reactivity and thermal stability of the formulation, especially related to high temperature printing adopted in the SLA Hot Lithography process. To assess these features, we tested epoxy linseed oil (ELO) in three systems containing I-SbF6 (with ITX as sensitizer to be active in the wavelength of laser emission of the printer), S-SbF6 and S-BF5 as photoinitiator. We study the reactivity by means of photo-DSC analysis at 100 °C. We have selected the best photoinitiator

investigating their reactivity at 100 °C since for all the studied photoinitiators we could observe a linear increase of reactivity and final epoxy group conversion by increasing temperature. The best performance for all the investigated photoinitiator were achieved at 100 °C, which is also a temperature suitable to avoid thermal activation. All these aspects will be further discussed in detail below. By comparing the photo-DSC data for the different photoinitiators, it is possible to highlight the best performance of S-BF5 due to the lowest t_{peak} and highest R_P compared to the other systems (see Fig. S1). However, all systems exhibited good reactivity at high temperature verified by the low t_{peak} below 20 s. The stability of the formulations was investigated by means of STA analysis of uncured samples to verify the thermal activation of the formulations (Fig. S1). Indeed, photoinitiators could also be activated by increment of temperature [36,55]. I-SbF6 showed an onset around 140 °C, S-SbF6 around 160 °C and S-BF5 around 170 °C meaning that printing around 100 °C ensures a pure UV-activated reaction. Nevertheless, thermal stability test at 100 °C were performed by keeping the formulations in isothermal condition to simulate the condition of the Hot Lithography process and evaluating the viscosity of the resin upon prolonged heating. The I-SbF6 turned solid in less than 24 h due to the thermal cross-linking taken place at high temperature (Fig. S1). High stability was reached by S-SbF6 which had a cross-linking within 3 days. However, the formulation containing S-BF5 was stable over 3 days keeping the liquid state with suitable viscosity for all the tested time. Considering the aforementioned results, we selected S-BF5 as best system to investigate the UV-curing process and the Hot Lithography of the bio-based composites. We continued the investigation with S-BF5 as photoinitiator added in 3 phr in all formulations listed in Table 1.

3.2. UV-curing process

The EVOs exploited in the Hot Lithography process react by UV-cationic curing process which involved the ring opening reaction of epoxies, as reported in Scheme 1. As can be seen, the activation of the photoinitiator generates a strong acid which starts the opening of the epoxy ring by formation of a carbocation. Consequently, this carbocation can open another epoxy ring starting the cross-linking reaction.

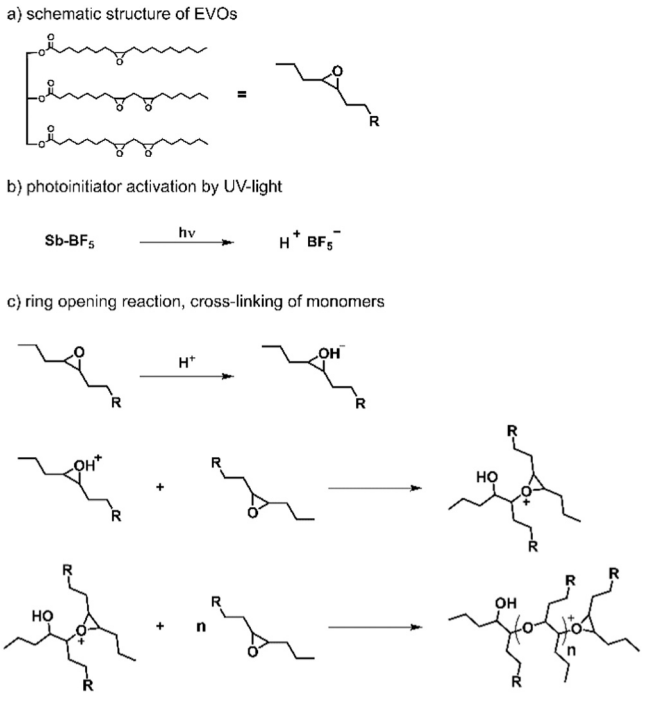

Scheme 1. UV-cationic curing reaction of EVOs; (a) structure of EVOs; (b) activation of PhI; (c) cationic reaction of epoxies.

Firstly, the investigation aimed to study the UV-curing process for the pristine bio-based epoxy vegetable oils at different temperatures by means of photo-DSC and photorheology. We selected 25, 50, 75 and 100 °C to investigate the temperature effects on the kinetics during the UV-curing process. The outcomes are highlighted in Fig. 1, where R_P and EC_{DSC} are reported in function of the temperature. The photo-DSC evaluation was done considering the epoxy number of the resins calculated by titration, 5.55 ± 0.10 and 4.36 ± 0.7 for ELO and ESO respectively, and verified through ^{1}H NMR (Fig. S2, 5.29 ELO and 4.22 ESO). We could observe an important enhancement of epoxy group conversion by increasing temperature reaching values over 90% for both vegetable epoxy oils employed at 100 °C. Moreover, it is clear that by operating at higher temperature indeed R_P increased significatively, going from about 25 mmol/s * L at 25 °C, up to 200 mmol/s * L when UV-curing was performed at 100 °C. All these data can demonstrate that by increasing temperature it is possible to facilitate the 3D printing of epoxy vegetable oils by increasing kinetic and conversion. The maximum rate was reached at 100 °C with 196 and 141 mmol/s * L for ELO and ESO respectively.

The conversion data were confirmed by ATR-FTIR analysis conducted at different temperatures between 25 °C and 100 °C. ELO spectra are reported in Fig. 2. As demonstrated by Photo-DSC analysis, The temperature had a massive influence over the conversion, showing an important enhancement of epoxy group conversion by increasing temperature. This is a well-known effect in cationic photopolymerization well described by Crivello [56] which showed that cationic epoxy ring-opening polymerization can be markedly accelerated when they are carried out at high temperatures. This is particularly true when the aliphatic epoxy ring are exploited in cationic photopolymerization since they create a stable intermediate structure during the ring-opening slowing down the curing speed. Polymerization does not proceed spontaneously at room temperature in such systems. However, if photopolymerization is performed at higher temperature, the ring-opening reaction starts much faster [56–58].

Indeed, the epoxy peak progressively disappeared passing from UV-curing performed at 25 °C to UV-curing at 100 °C proving an increment of the conversion operating at high temperature. The consistency with the results from the photo-DSC can be considered as good and all the data are listed in Table S1. The ATR-FTIR analysis was also conducted also for ESO-based thermoset UV-cured at different temperature and reported in Fig. S3. The analysis confirmed the same trend of enhancement of conversion upon increment of curing temperature.

Finally, photorheology was performed at different temperatures (Fig. 3 A) to investigate the formation of the epoxy network and the

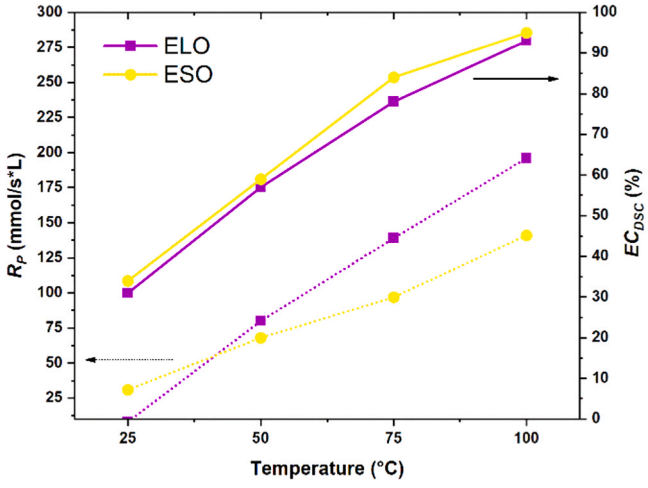

Fig. 1. Photo-DSC results: Rate of polymerization (R_P) and epoxy conversion (E_{CDSC}) in function of the temperature for ELO (purple lines) and ESO (yellow lines).

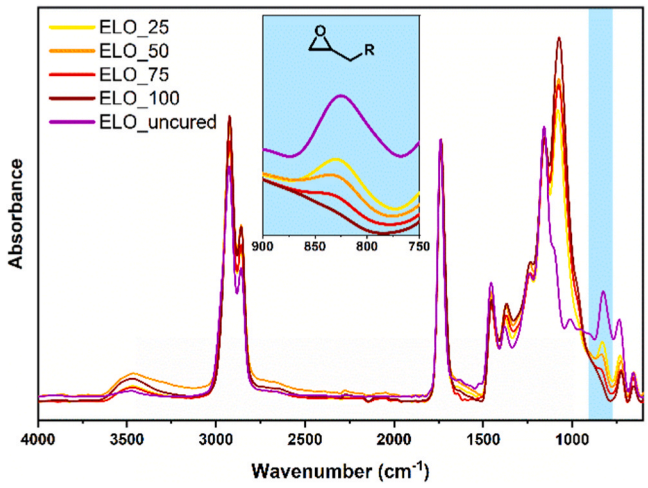

Fig. 2. ATR-FTIR spectra of ELO UV-cured at different temperatures (25, 50, 75 and 100 °C) and the spectrum of the uncured formulation (purple line). The formulation contains 3 phr of S-BF5.

trend in the t_{gel} which is defined at the intersection between Storage modulus (G') and Loss modulus (G''), highlighted in Fig. 3B. This important parameter allows to understand the time required to form a solid network. Moreover, it is an indication for the setting of printing parameters to be able to have a self-sustain layer which does not collapse during the additive manufacturing process. By increasing the temperature, it is evident a decrease of t_{gel} from 16.0 ± 1.0 s at 25 °C to 4.5 ± 1.5 s at 100 °C for ELO. The decrease was more accentuate for ESO with a variation of about 20 s in t_{gel} between the curing process at 25 °C and at 100 °C (Table S1). The trend in G', recorded for ELO, is reported, as an example, in Fig. 3 A. Indeed, a clear decrease in the induction time is evident by increasing temperature. Moreover, an increase in the slope can be observed, confirming the faster kinetic at higher temperature. The same investigations were performed also for ESO and reported in Fig. S4. The trend registered for ESO was in agreement with the result of ELO above discussed.

3.3. Filler influence on UV-curing process

Considering the epoxy group conversion reached operating at 100 °C and the faster kinetics, we selected this as printing temperature for the Hot Lithography 3D printing process. In order to investigate the effect of the different fillers in the UV-curing, photo-DSC analysis was performed for all the formulations containing the different amount of fillers. The results highlighted that the fillers did not significantly affect the final conversion. All the formulations reached over 80% of EC_{DSC}. Noticeable high conversion was reached by formulation containing H200 (Table S2). This could be explained taking into consideration that the fillers surface containing a high number of OH-groups which can interact with the carbocationic growing chain via a chain transfer reaction, with a consequent enhancement of the final epoxy group conversion [59]. The proposed mechanism is illustrated in Scheme 2, where the chain growth mechanism of cationic UV-curing is presented comparing the chain transfer reaction that take place between the polymer matrix and the filler. The presence of OH was verified by ATR-FTIR analysis of the fillers, where it is visible the OH band in the region of 3500 cm^{-1} as presented in Fig. S5.

The presence of the filler should hinder the curing process because of competitive absorption with the photoinitiator and decrease of available UV-light intensity [60]. Nevertheless, the chain transfer process, induced by the OH groups present on the filler's surfaces, will counterbalance the decrease of the photogenerated acid, inducing an enhancement of the curing process [61,62]. The two phenomena are somehow balanced and for this reason the overall UV-curing is not significantly affected by the present of the filler in the photocurable formulations.

The fillers WS200 or WS325 reduced more significantly the R_P with respect to the fillers H200 and T200 which can be explained considering the nature of the fillers. Strong brown color for the wall nutshell powder can generate a strong obstacle for the UV-transmission while white fillers like tagua and hemp could affect less the light intensity penetration depth. Fig. 4 reports the photo-DSC analysis of the formulation containing different amount of H200. The trend of R_P (proportional to the h_{peak}) is clear as well as the decrease of the total ΔH release during the reaction. The formulation containing 20 phr of H200 had the lowest conversion, 55% EC_{DSC}, which was also attributed to the higher viscosity reached for this formulation. The high viscosity limited the propagation of the carbocationic growing chains. This relevant feature drives the attention to another crucial parameter for the printing which is the viscosity. The formulations suitable for SLA need to have proper viscosity to flow forming homogeneous layers on the vat for each platform movement. The viscosity was measured at printing temperature, 100 °C, and most of the formulations had appropriate value which were kept over 6 days confirming the stability of the formulations in the printing conditions (Fig. S6). A standard value lower than 20 Pa*s can be considered as indication of limit to be able to print [36,55]. The

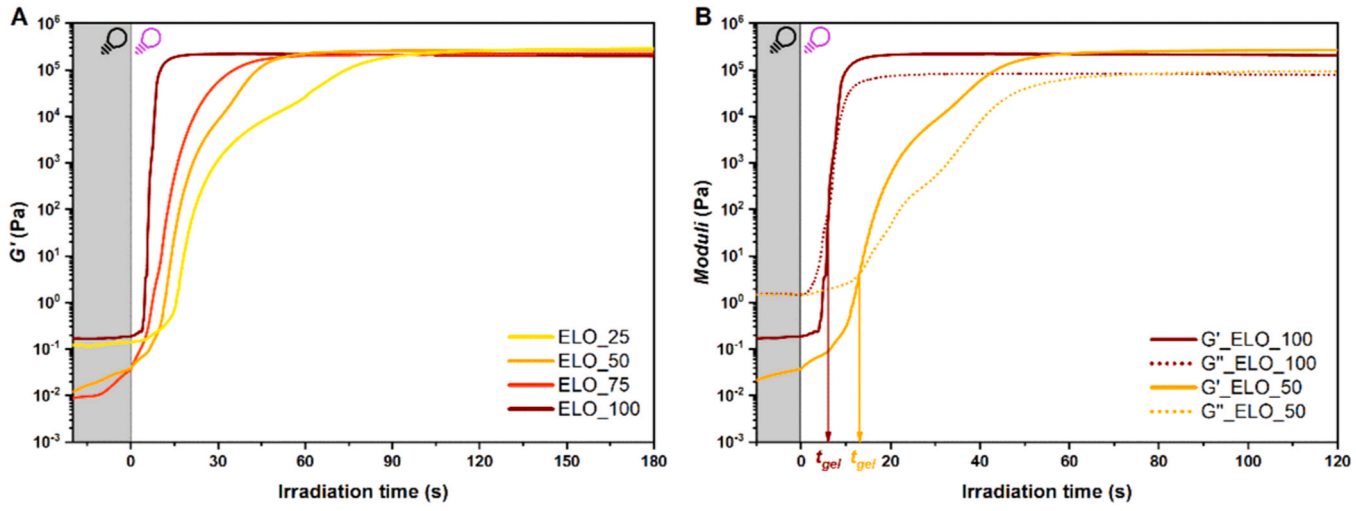

Fig. 3. (A)Storage modulus (G') of ELO in function of the UV-irradiation time at different curing temperature; (B) Representative moduli curves (G', solid lines, and G'', dot lines) of ELO recorded at different temperature: 100 and 50 °C.

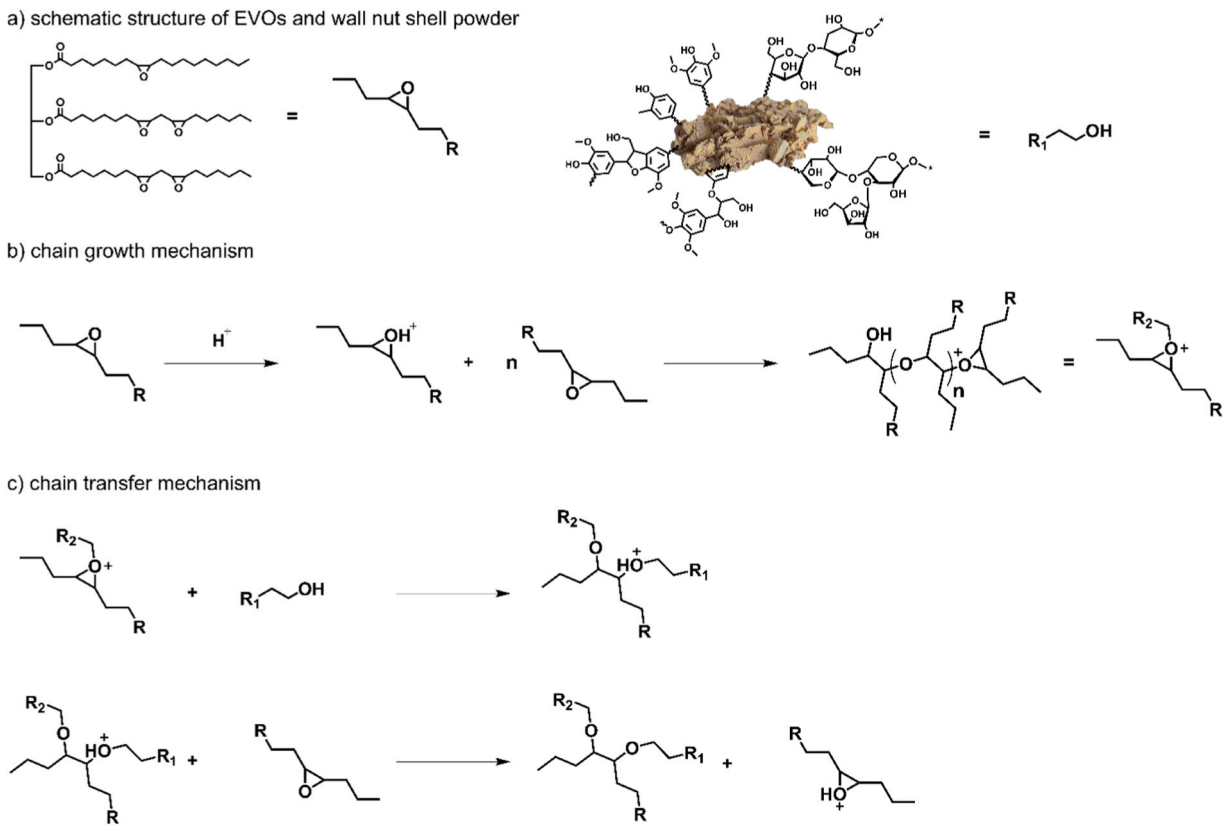

Scheme 2. Illustration of chain transfer mechanism. (a) schematic representation of epoxy vegetable oils and wall nut shell powder; (b) UV-cationic chain growth mechanism; (c) chain transfer mechanism which can happen between the polymer growing chain and the filler.

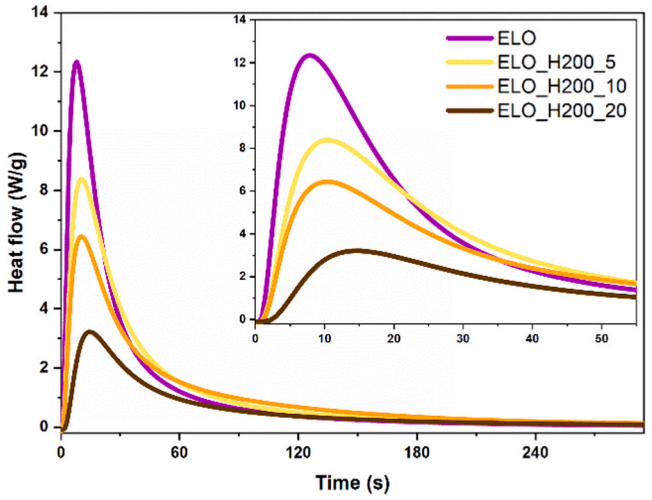

Fig. 4. Photo-DSC thermogram of the formulations containing ELO as epoxy vegetable oils and H200 as fillers in different amount.

ELO_H200_20 was not suitable for the printing due to the higher viscosity and the difficulty to properly flow, so we did not further investigate this specific formulation and we limited for UV-curable formulations containing 5 and 10 phr of H200 as filler. The reason of the higher viscosity can be attributed to the filler geometry. Specifically, the filler shape had a main role in the viscosity enhancement. Indeed, the wedge-shape of hemp generate a strong increase in the viscosity varying from 5 to 20 phr (Fig. S7) which generate a limitation in the filler addition into the resin. The other fillers had a lower impact on the final viscosity of the formulations allowing the addition of 20 phr. The reason could be due to the more round-shape geometry of wall nutshell and tagua. The filler morphology was investigated by SEM analysis reported in Fig. S8.

Whitin the thermal stability of the resin, the dispersion and the stability of the fillers was evaluated and reported in Fig. S9. The high temperature produce a decrease of viscosity which lead to sedimentation of the filler over the time. The analysis showed a good stability up to 8 h, later the sedimentation start to be imponent. In the view of prolonged printing, the mixing of the resins is required to ensure a proper dispersion. However, the coating units of the printing guarantee a proper mixing of the resin within the tested geometries as successively confirmed by image analysis where an homogeneous distribution of the filler is present.

To confirm the photo-DSC data, ATR-FTIR analysis and photo-rheology test were carried out on the epoxy UV-curable formulations with the highest amount of filler to investigate the final conversion ($EC_{ATR\text{-}FTIR}$) and a possible delay in the t_{gel} which should be considered in the setting parameters for additive manufacturing. Fig. S10 and Table S2 report the results underlining the similar value of conversion and the t_{gel} compared to the result obtained for the pristine formulations. $EC_{ATR\text{-}FTIR}$ was in agreement with the conversion calculated by photo-DSC confirming the efficiency of the UV-curing process also when the fillers were added into the formulations. Instead, photo-rheology test revealed that the ELO-based filled formulations had an increment in t_{gel} of about one second with respect to the pristine formulation while the ESO-based formulations had only 0.5 s enhancement. This means almost no influence of the filler in the UV-curing process at given amount confirming the feasibility of the additive manufacturing. The photo-rheology results were in accordance with the photo-DSC outcomes which previously highlighted the similar range of R_P meaning a fast reaction also for the epoxy formulations containing fillers.

The last validation of the successful UV-curing process was done by

STA analysis on the cured composite to investigate a possible residual curing and the need of subsequent thermal treatment (Fig. 5). The UV-cured sample did not exhibit any exothermic peak, meaning that the UV-irradiation at 100 °C was enough to ensure a complete epoxy group conversion. The formulation containing 20 phr of WS200 showed a minor exothermic peak around 150 °C which can be due to the incomplete epoxy group conversion. From STA analysis it was also possible to confirm that the filled UV-cured samples revealed a thermal stability over 250 °C confirmed by the low weight loss up to this temperature. T_{95} varied from 270 and 290 °C for the tested composites.

3.4. 3D printing Hot Lithography and mechanical testing

The vegetable epoxy oils were used as photocurable resins for the preparation of bio-based composites with the bio-based fillers as describe in Table 1. The Hot Lithography was performed for all the different formulations. Specifically, DMTA and tensile specimens were printed at 100 °C with a layer thickness of 100 μm for each layer (Fig. S11). Firstly, we were able to print not only the pristine epoxy oils, but we achieve to 3D printing bio-based composites. For the best of our knowledge this interesting result achieved with epoxy monomers it is not described in literature and it open the possibility to increase the portfolio of the bio-based materials which can be used to substitute fossil-based resins and composites. Moreover, the employing of bio-based fillers further increased the total amount of bio-derived products. This showed the possibility to successfully employ bio-based fillers originated from industry side-stream for 3D printing applications. The Hot Lithography investigation was conducted to verify the possibility to develop complex geometry to fulfill the aim of the additive manufacturing which in most cases it has been employed to developed complex, self-sustain structure which cannot be made with other process techniques. Fig. 6 showed some result achieved with ELO-based composite printed with the highest amount of different type of fillers, from wall nutshell to hemp. The good reproducibility and the accuracy of the 3D printing were tested by morphology and surface analysis employing either microscopy analysis, by optic and SEM analysis, or 3D scanning analysis. Pictures of 3D printed objects were taken at different magnification to investigate the surface revealing a good response of the resins testified by the good reproducibility of the geometries. Considering the hexagonal net, illustrated in Fig. 6D, image analysis was carried out measuring three different geometry's dimensions. The hexagonal hole had a diagonal (a) of 3.782 ± 0.030 mm while the wall thickness (b) was 0.361 ± 0.035 mm. Furthermore, it was possible to evaluate the layer thickness (L) by the magnification at 20 × performed on the side of the net, revealing an average of 102 ± 5 μm which was in accordance with the set value of 100 μm used for the Hot Lithography 3D printing.

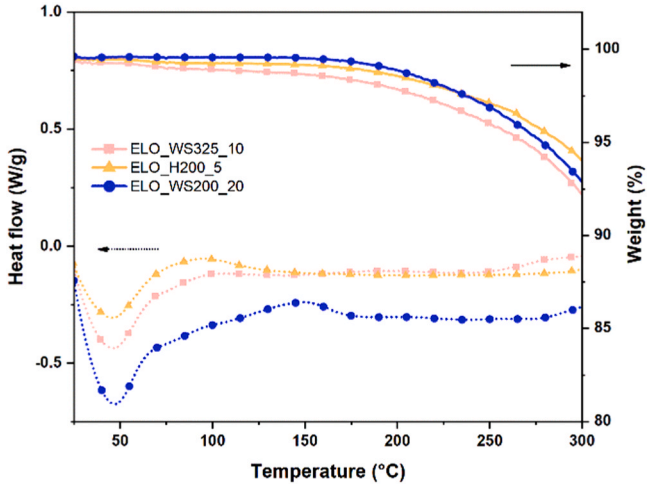

Fig. 5. STA analysis of three ELO-based composite containing WS325, 10 phr (red line); H200, 5 phr (orange line); and WS200, 20 phr (blue line).

However, from the Fig. 6, it is visible how some net's edges reveal some imperfections probably due to the presence of the filler and the relative scattering and absorption phenomena which can limit the accuracy of the 3D printed geometries. To verify this important feature of the resins used in the Hot Lithography, SEM analysis of the surface (Fig. 7) and 3D scanning analysis was performed. SEM analysis highlighted the edges of two different 3D printed nets and the surface of the pyramid. From these images the scattering problem of the filler are visible, however the good structure of both structure is shown. Furthermore, the 3D scanning analysis allowed the comparison between the CAD file used to create the object and the three-dimensional model of the 3D printed object (Fig. 8). An overlay map can be created to define the accuracy and the precision of the geometry with respect to the starting CAD file. The best performance was attributed to the ELO_WS325_20 with a green zone of about 38% meaning a high accuracy in the selected range of ± 50 μm. The other resins were less accurate with value around 20% (Table 2), however the mean values as well as the variances were tight and narrow for all the objects demonstrating a good reproducibility of the CAD file. ELO_H200_10 had the lowest mean value with 0.0637 mm. The discordances and irregularities can be attributed to several factors. Firstly, the resin limitation can explain part of the errors due to the presence of the filler which generate scattering and absorption phenomena hampering the light path. Then, some process-dependent errors such as printer resolution, printing errors and scanner precision could affect the result. Artefacts could be also created by the inhomogeneous distribution of magnesium stearate used to increase the efficiency of the 3D scanner as well as the presence of the support (visible in Fig. 8) which enable a correct acquisition of the imagines. As future prospective, the creation of proper printing formulations with dye and inhibitors of cationic UV-curing to maximize and optimize the light absorption could lead to increase the accuracy and precision of the 3D printing objects.

The thermo-mechanical properties of the composites were investigated by DMTA analysis. Pristine ELO and ESO showed a different T_g which can attribute to the different epoxy value of the oils. Indeed, high epoxy value mean to reach higher cross-linking density and therefore higher final rigidity of the polymeric network. ELO had an epoxy value of 5.55 while for ESO was 4.36 therefore ELO reached a T_g of 47 °C while ESO had a T_g of 7 °C (Fig. 9 A). This result confirms the possibility to tailor the properties of the crosslinked polymeric network, simply playing with the epoxy value. Indeed, ELO had a ν of 4300 mmol/dm^3 compared to 1835 mmol/dm^3 for UV-cured ESO. The large availability of several epoxy vegetable oils allows to have a wide range of starting properties that can be tailored according to the application requirements as previously demonstrate for coating applications [63]. Interesting thermo-mechanical response was reached by Hot Lithography compared to the traditional stereolithography. Indeed, in a previous investigation conducted by Branciforti et al. [64], the maximum achieved T_g exploiting EVOs in 3D printing was about – 26 °C. The use of Hot Lithography showed best result in terms of kinetic and conversion confirming the beneficial effect on the mechanical performances.

The next step was the investigation of the effect of the presence of the bio-derived fillers into the pristine epoxy oils. Interestingly, the filler did not particularly affect the final T_g of the network. As we previously discussed, the presence of the filler did not significantly hinder the UV-curing allowing the proper formation of the network and this was attributed to the chain transfer mechanism. When adding a reinforcing filler, we should expect an enhancement of the T_g due to the hindering of the mobility of the polymeric network. In our case this mobility hindering is counterbalanced by the expected decrease of crosslinking density attributable to the chain transfer reaction. As a final results, the addition of the filler did not significantly affect the final T_g of the cured materials. The result reported in Fig. 9B confirmed that the filled UV-cured formulations containing 10 phr of the different fillers, showed

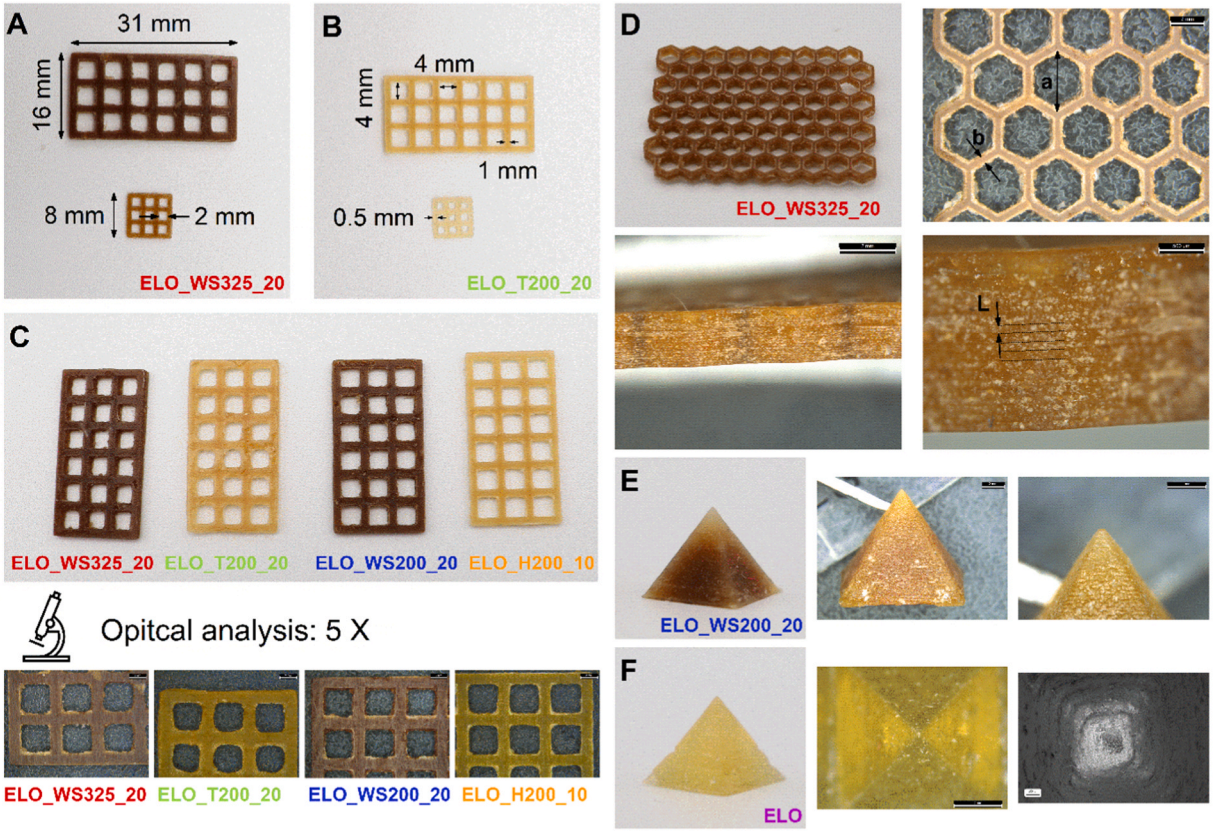

Fig. 6. 3D printed specimens by Hot Lithography performed at 100 °C. Each layer was 100 μm. (A, B, C) 3D printed net ELO-based with the different fillers in the highest amount; (D) honeycomb net made of ELO_WS325_20 (total volume of 70 ×40×4 mm) with optical analysis; (E) squared-based pyramid of ELO_WS200_20 with optical images at 5 × ; (F) ELO-based pyramid with optic and SEM images at 10 × and 100 × respectively.

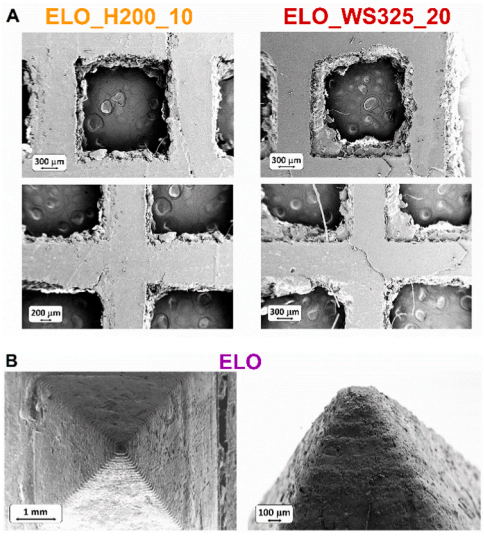

Fig. 7. SEM analysis of the surface of the square grids and ELO-based pyramid to highlight the morphology of the 3D printed samples. The images of grid are 30 × while the pyramid images are at 20 and 70 × . The pseudo backscattered detector SE2 has been used with collector bias at 0 V.

almost the same T_g of the pristine UV-cured resin. We complete the DMTA characterization performing the analysis for the composites with highest amount of filler (20 phr) and for the ELO_H200_5. The trend of G' and the *Tan* δ are reported in Fig. S12. The ESO-based composites were also tested. The maintenance of the T_g of the epoxy polymer ESO matrix was confirmed as reported in Fig. S13.

Furthermore, we investigated the tensile properties of UV-cured biobased composites in order to verify a possible influence of the filler's presence. Firstly, tensile test was carried out on the 5B type dog bone 3D printed of the pristine ELO and ESO epoxy resins. The results corroborated the DMTA analysis since the epoxy vegetable oil with the highest epoxy value, ELO, showed the best mechanical performance as reported in Fig. 10 A. The highest epoxy content gave high rigidity to the network and the best mechanical performance in terms of final strength. Crosslinked ELO showed a strength of 10 MPa compared to 1.1 MPa given by the crosslinked ESO epoxy resin. The E increased from 0.27 MPa for UV-cured ESO to 3.30 MPa for crosslinked ELO.

The addition of the filler affected all the properties, E, σ, ε and U. Fig. 10B reports the tensile curves recorded for the UV-cured composite containing 10 phr of the filler compared with the pristine ELO. The filler increased the strength of the composite giving more rigidity as confirmed by the increase in Young's modulus. Tagua and Hemp achieved higher values of E and σ which can be reconducted to the intrinsic shape features of the fillers. Indeed, Hemp was the wedge-shape filler which can influence differently the final composite properties. Furthermore, it is interestingly how the filler dimension can affect the properties. Comparing the wall-nut shell composites (WS200 and WS325) we can discuss the influence of the mesh 200 and 325. It is clear how the higher dimension of the filler can contribute to reach higher strength at break, but with a consequent decrease of the elongation due to the higher rigidity given to the composite.

We can also prove a trend in the tailoring of the properties by playing with the amount of the added filler. The Fig. 10 C reports the representative tensile curves for the UV-cured ELO epoxy resin containing WS325 as a filler with a content of 10 and 20 phr respectively. It is clear how increasing the filler content from 10 to 20 phr (or 5 to 10 phr for H200) we could each an increase in E, σ, and U as reported in Table S3.

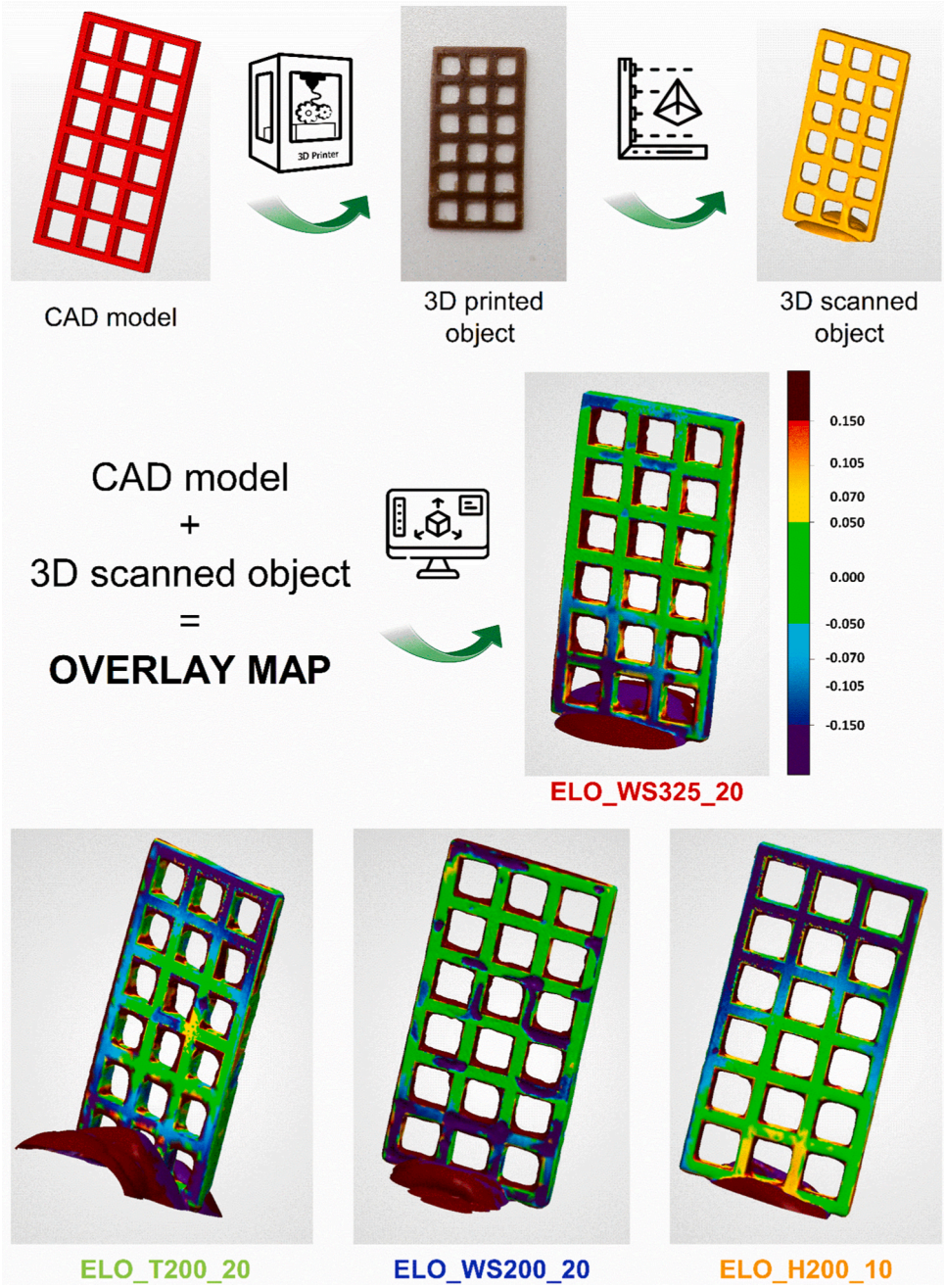

Fig. 8. Overlay maps created by 3D scanning analysis of the ELO-based 3D printed square nets with the different fillers. From the CAD model to the 3D printed object to evaluate the accuracy of the printing.

Table 2
Data of 3D scanning analysis of the different ELO-based 3D printed square nets.

ENTRY	Mean value (mm)	Variance (mm)	ST deviation (mm)	Green zone (%)
ELO_H200_10	0.0673	0.0341	0.1846	23.84
ELO_T200_20	0.1336	0.0893	0.2989	21.85
ELO_WS200_20	0.1369	0.0389	0.1972	22.90
ELO_WS325_20	0.0883	0.0395	0.1987	38.31

Previous results reported in literature for bio-based thermoset originated from acrylated vegetable oils reinforced with nanocellulose showed strength value around 6 MPa employing micro and nanocellulose [65]. Better results were obtained combining the acrylated epoxidized soybean oil (AESO) with pristine nanocellulose and acrylated nanocellulose reaching a maximum of 10 MPa [47]. A further study showed a similar behave with a low content of nanofibrillated cellulose [66]. Thus, the innovation using an epoxy vegetable oil matrix in synergy with bio-derived filler permitted the achievement of better mechanical properties with value around 15 MPa. The highest toughness was achieved for ELO_WS325_20 with 2950 Jm^{-3} which was 8 times higher than the toughness of pristine ELO. This represent again an interesting value being 4 times higher with respect to others reported in literature [66]. However, the lack of detailed studies with epoxy-based resin due to the focus in acrylate-resins makes this result a prominent outlook for further developments. The stress-strain curves for all fillers are reported in Fig. S14 revealing the same trend discussed for WS325 and the result of the ESO-based composite are reported in Fig. S15.

Gel content analysis on 3D printed thermosets was performed to validate the investigation of the UV-process performed by STA analysis

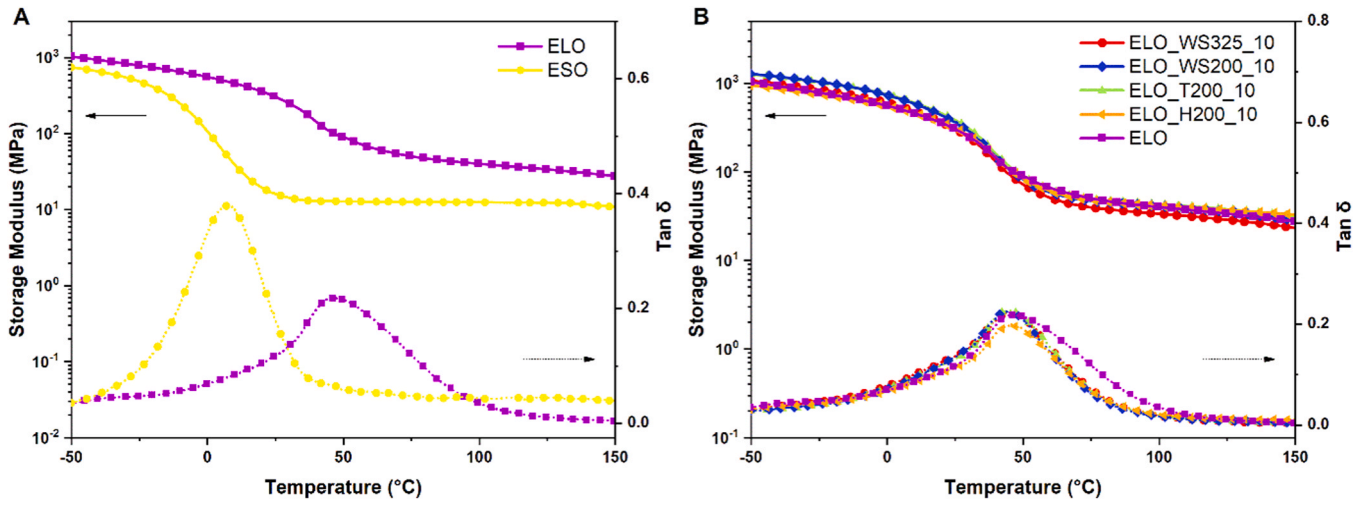

Fig. 9. (A) DMTA of pristine ELO and ESO 3D-printed at 100 °C; (B) DMTA of ELO-based composites with 10 phr of the different filler used in the study.

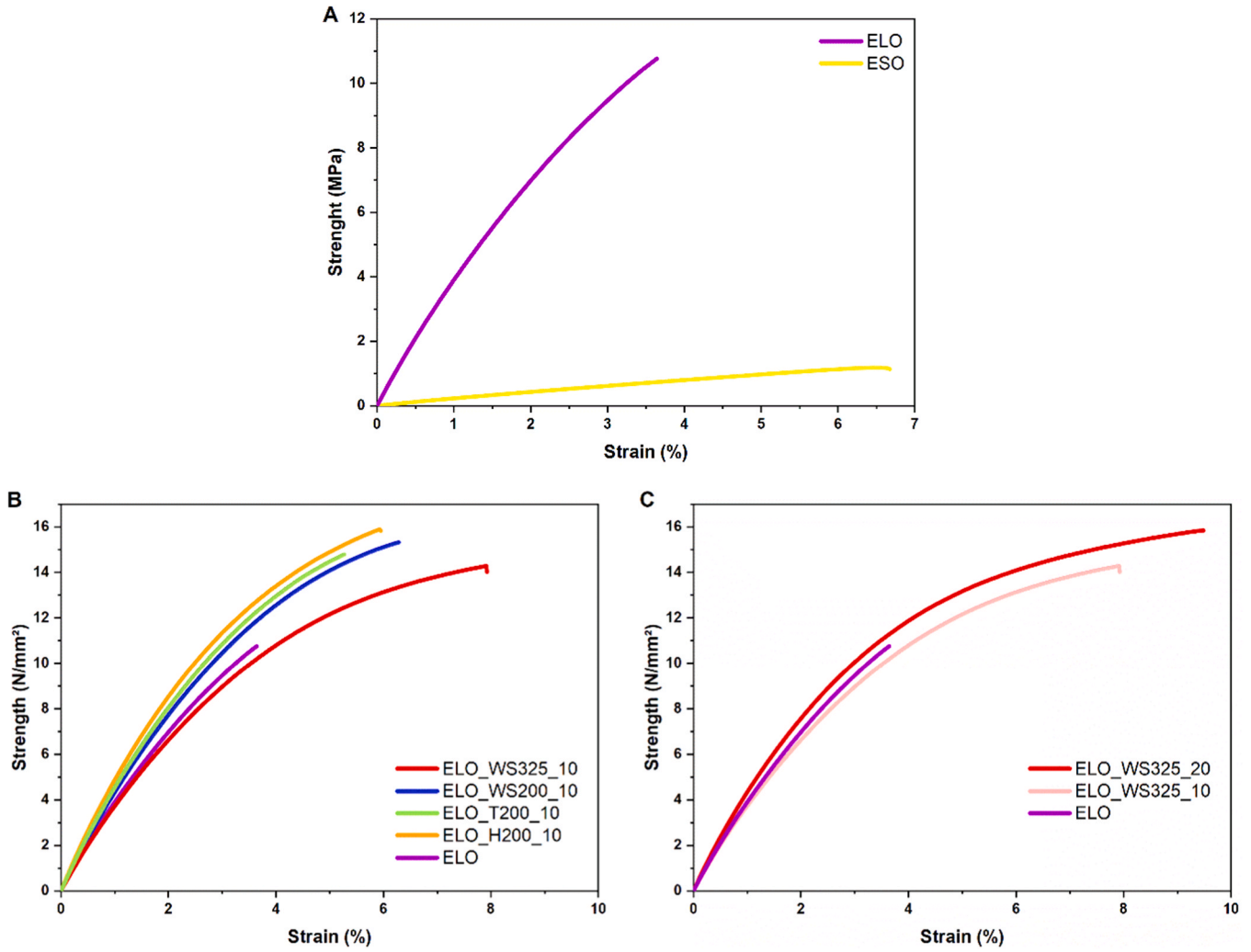

Fig. 10. (A) Tensile test performed on 3D printed specimens of ELO (purple line) and ESO (yellow line), representative curves of 5 different test are reported, the average values are listed in Table S3; (B) Tensile test of the 3D-printed specimens (representative curves are presented). Effect of addition of 10 phr of WS200, WS325, H200 and T200 to ELO; (C) Tensile test of composites containing WS325 in the two tested amount, 10 phr and 20 phr.

(Paragraph 3.3). Indeed, by this method it is possible to verify the formation of cross-links which originate an insoluble network. Hot Lithography can allow the elimination of post thermal treatment due to the reaching of complete conversion in the frame time of the 3D printing job performed at high temperature. The high gel content of 98% and 93% for ELO and ESO respectively demonstrating the formation of insoluble network by Hot Lithography 3D printing. The possible limitation of the epoxy conversion impacting on the formation of a proper network by the presence of the filler has been assessed by gel content on 3D printed composites with the highest amount of fillers. The outcomes, reported in Table S3, highlight value over 90% for all the ELO-based thermoset revealing a proper formation of the network. The same trend has been observed for ESO-based thermoset with value ranging from 88% to 91%.

3.5. Matrix-filler interface investigation

Interestingly the wall-nut shell filler added to the polymer matrix exhibited the best behave in terms of *U* (i.e., the toughness can be evaluated ad the area under the stress-strain curve) when it was used in the content of 20 phr for ELO epoxy resin. The presence of the fillers had astonishing effects in terms of mechanical properties of the composites. Therefore, we investigated the origin of this benefit. As previously demonstrated by ATR-FITR analysis, the surface of the different filler showed OH groups (Fig. S5). These functional group derived from cellulose, hemicellulose and lignin (main components of the bio-derived fillers) could interact with the epoxy matrix through the chain transfer reaction, as reported in Scheme 2. The chain transfer mechanism can allow the chemical bonding between matrix and filler. This can be directly translated into a strong interaction between polymer and filler which could contribute to the important enlacement of the final properties of the composites. To confirm this hypothesis, we functionalized the WS325 filler via silanization process. The reaction step allowed to react most of the OH groups on the surface generating Si-O links (Fig. 11). The validation of this step was performed by ATR-FITR analysis. The spectra pre and post functionalization verified the reaction by the presence of the $Si(CH_3)_3$ peak and the decrease of the OH peak as reported in Fig. 12. SEM analysis was performed on the silanized particles to investigate the morphology and the size of the particles (Fig. S16) revealing an average dimension of 34.4 ± 11.5 μm. By distribution analysis it was possible to state that 87 ± 1% of particle had an average size below 45 μm as the pristine particles, thus the treatment did not influence the size distribution acting only on the chemical bond on the surface which appeared more jagged.

The modified WS325 filler was used for Hot Lithography of DMTA and tensile specimens to test and verify the influence of the interaction between the functionalized bio-derived filler and bio-based epoxy polymer matrix. Fig. 13 A reports the comparison between the ELO UV-cured composite containing WS325 unmodified filler and WS325 silanized filler at 20 phr content. It is evident a slightly decrease of the T_g (of about 5 °C) for the ELO_WS325_20_SIL which could be addressed by a poorer filler-matrix interaction. A further confirm of the decrease of the properties due to the surface modification was the stress-strain curves reported in Fig. 13B for the ELO UV-cured composites The poorer interaction between polymer and filler affected the final properties decreasing *E*, *σ*, and *U*. Specifically, the *E* varied from 4.6 for the ELO UV-cured composites containing the original WS325 filler at 20 phr, down to 3.3 MPa for the same ELO composites containing the same amount of the silanized filler. As well we could observe that the strength was reduced from 16.8 for the 3D printed composites containing the original filler down to 8.6 MPa for the composites containing the silanized filler. Finally, the toughness decreased 10 times when the silanized filler was dispersed in the UV-curable epoxidized vegetable oil, as can be clearly seen by the area under the stress-strain curves. Thus, we can validate the benefit of the presence of the OH groups on the surface of the bio-derived filler which allowed a good chemical interaction at the interface providing advantages in the composites. This advantage played a crucial role on the properties with respect to the possibility to increased compatibility between filler and matrix due to surface modification. Indeed, in previous articles the benefit of interaction between epoxy and cellulose-based filler has been reported [67,68].

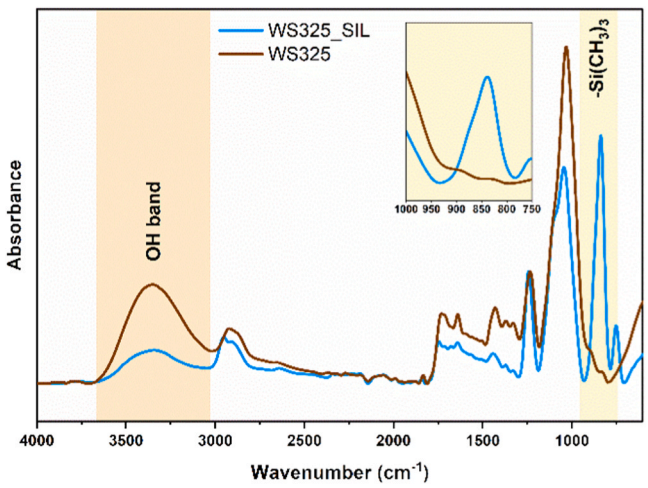

Fig. 12. ATR-FTIR analysis performed pre and post reaction on the WS325 powder.

3.6. Morphology of the composites

The samples derived from tensile analysis were used to investigate

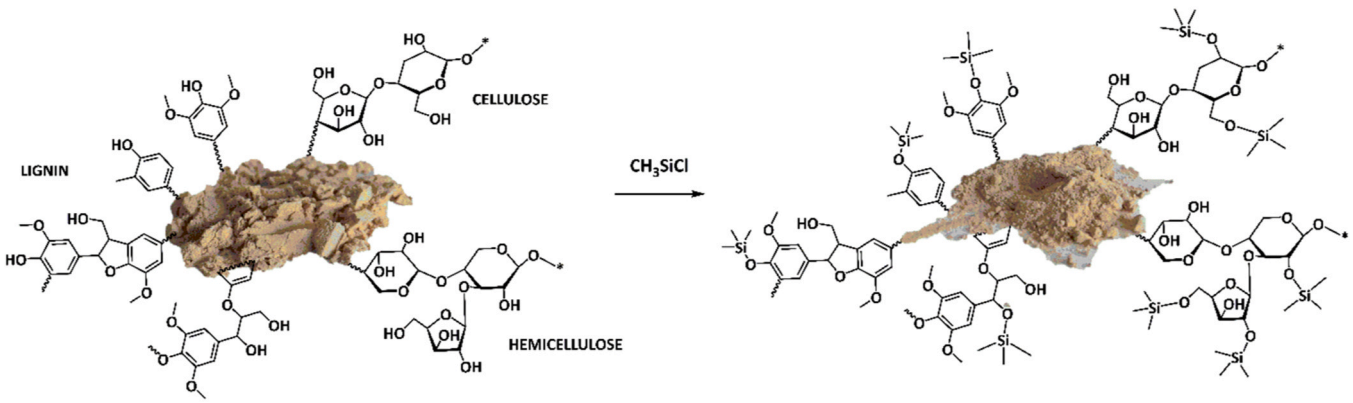

Fig. 11. Representation of the silanization step done on WS325.

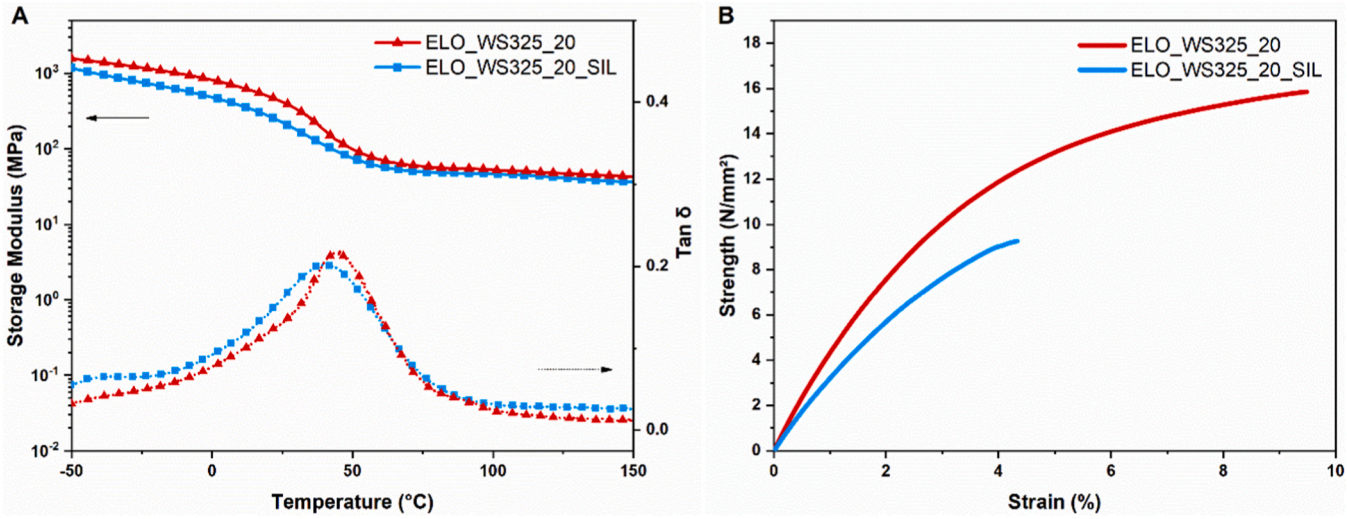

Fig. 13. (A) DMTA of ELO_WS325_20 and ELO_WS_325_20_SIL; (B) Tensile test of ELO_WS325_20 and ELO_WS325_20_SIL, representative curves of each thermoset are reported.

the morphology of the composite to evaluate the distribution of the filler into the 3D printed specimens as well as the interaction between the filler and the matrix. Fig. 14 reports the difference between the ELO_WS325_20 and ELO_WS325_20_SIL. It is clear how the fillers were homogeneously distributed into the composite without any agglomerations or sedimentations. Furthermore, the analysis of the interface of ELO_WS325_20_SIL highlighted the problem of compatibility between matrix and filler. Indeed, some voids between matrix and filler were visible at high magnification. This could be originated from the poor interaction of matrix-filler, and they could also explain the result of the weak tensile properties reported in Fig. 13. Looking into the interface between unmodified WS325 and ELO we could see a strong interaction confirmed by the lack of voids and the presence of a homogeneous distribution along the thickness of the sample. Moreover, a complete SEM analysis of the fractures is reported in Fig. S17. The comparison between the pristine ELO and the composites containing 10 phr of the different fillers was carried out. This highlighted the homogeneous distribution of the powders and the good interface with all the bio-derived fillers, from hemp to tagua. The analysis was carried out on ESO and derived composites which showed the same good result expressed for ELO. The distribution and the interface were as good as ELO-based composite. Lastly, it was also possible to see the different printed layers which were in the range of 100 μm according to the setting 3D printing parameter of the Hot Lithography (Fig. S17).

3.7. Chemical degradation of the composites

The bio-based composites were chemically degraded to prove the possibility to decompose the polymer matrix in a possible circular economy view. The polymer matrix could be reused to further produce other materials. This proof of concept was carried out in a strong alkaline environment at high temperature to accelerate the degradation process. The degradation was followed through the time by mass loss analysis. It is important to highlight that the strong alkaline condition had also an effect on the bio-derived fillers since they are mainly composed by cellulose, hemicellulose and lignin. Indeed, these natural monomers are degraded under strong alkali conditions [69,70].

Fig. 15 presents the chemical degradation of the composites which was accentuate for the ESO-based composite due to the high

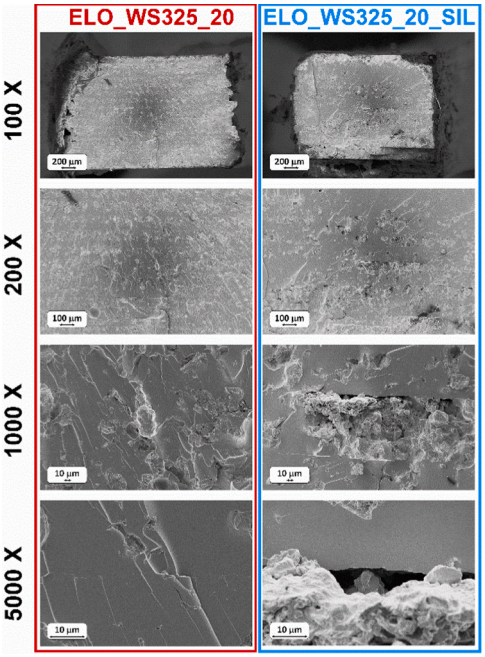

Fig. 14. SEM analysis of the composites derived from tensile test.

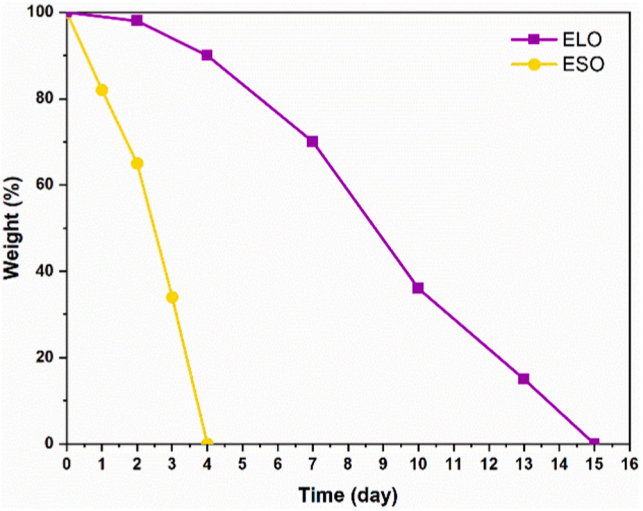

Fig. 15. Mass loss of the ELO and ESO in alkaline environment.

temperature of the treatment (80 °C). ESO had a T_g OF 7 °C which was much lower than the temperature used for the treatment. The increase mobility in the rubbery state could accelerate the degradation process. Indeed, the ELO degraded slower that ESO-based composites. The high cross-link density could help the resistance of the ELO which required up to two weeks to complete dissolve in the alkaline condition. The bio-derived composites showed a similar trend with respect to the pristine matrix (Fig. S18). The presence of the bio-based fillers in the ESO-based composites containing 20 phr slightly accelerated the weight loss due to degradation of the filler itself. Indeed, taking into consideration ESO, ESO_WS325_10 and ESO_WS325_20 it is possible to see an increase velocity in the degradation by increasing the amount of filler. Fig. S19 reports the degradation for ESO and ESO_WS325_10 in which is visible the degradation of the 3D-printed samples followed by the turning color of the alkaline solution.

The decrosslinking of the polymer network was originated by the ester bond leachability in NaOH environment [71]. ^{1}H NMR analysis on the final ELO degraded product (Fig. 15A) was carried out to confirm the hydrolysis of the ester bonds in the alkaline environment. It is possible to see the disappearance of the epoxy peaks (around 3 ppm) in the degraded product due to previous step of UV-curing. The characteristic glycerol peaks in the region between 4.5 and 4 ppm disappeared due to the hydrolysis of the ester bonds. Finally, it is possible to observe the formation of the acid derived from the ester hydrolysis. We supported the ^{1}H NMR analysis with ATR-FTIR analysis comparing the pristine ELO, the UV-cured epoxy resin, and the degraded product. The result is presented in Fig. 16B where three different regions were highlighted. The epoxy peak disappeared after the curing as previously demonstrate due to the cross-links. This originated ether linkages which can be founded in the UV-cured ELO and also in the degraded product around 1070 cm^{-1}. Interestingly, the ether region at 1160 cm^{-1} presented a decrease of the peak from ELO to ELO-degraded due to the breaking of the ester bonds of the glycerol linkage. Indeed, the peak of the C═O of the ester bonds at 1737 cm^{-1} shifted towards low wavenumber due to the formation of the acid in the degrade product (1708 cm^{-1}). With these analyses we proved the possibility to recover a degraded thermoset which could be useful for a polyester production in the view of a possible reutilization of degraded product derived from 3D printed composites.

4. Conclusions

The present study opens the possibility to exploit additive manufacturing for bio-based epoxy composites. The Hot Lithography process allowed to increase the reactivity of the epoxy vegetable oils reaching the opportunity to properly use additive manufacturing to print complex geometries. The gel time of ELO-based resins decreased passing from 16 s at 25 °C to 4.5 s at 100 °C confirming the benefit of operating at high temperature to proper exploit AM. The UV-curing process was deeply studied to find the best parameters and conditions to optimize the 3D printing. Indeed, the accuracy and fidelity, assessed by 3D scanning analysis, revealed a good match between the CAD model and the 3D printed composites. We investigated the effect of the matrix employing ELO and ESO as bio-based epoxy resins characterized by different epoxy content value. Indeed, the T_g of the thermoset was massively influenced varying from 7 °C for ESO to 47 °C for ELO which had an epoxy value of 4.36 and 5.55 respectively. Hence, we demonstrated the importance in the choice of the epoxy matrix to obtain the requested thermo-mechanical properties of the crosslinked materials. Several bio-derived fillers from wall nutshell to hemp were used to increase the mechanical properties of the crosslinked epoxy matrix with a successful result in terms of rigidity and toughness enhancement. We verified the effect of filler content, morphology and dimension investigating four different types of bio-derived fillers. The thermoset reach strength values above 10 MPa which are comparable or even better of those reported for acrylated-based 3D printed resins. The addition of WS325 showed the best performance reaching astonishing value of

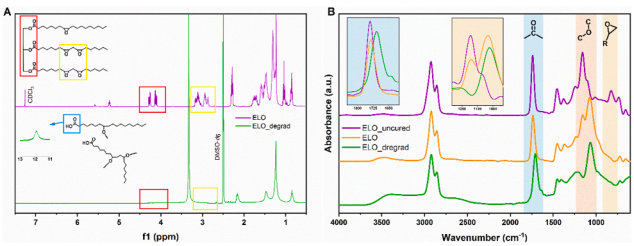

Fig. 16. (A) ^{1}H NMR analysis of uncured ELO (purple spectra) and degraded ELO (green spectra) with highlighted peak changing. Epoxy groups (yellow box), glycerol (red box), acid (light blue box); (B) ATR-FTIR spectra of ELO_uncured (purple), ELO UV-cured (orange), and ELO_degrad (green spectra) with zoom into the epoxy, ether and carbonyl region.

toughness with an increment of 8 times with respect to the pristine 3D printed ELO. Then we demonstrate the strong impact of the matrix-filler interface by silanization of the filler and comparison of final properties. This study revealed an important decrease of the properties due to the surface treatment since the chain transfer mechanism was hindered. Finally, we proved the possible chemical degradation of the thermoset in alkaline environment with a possibility to have a side product which could be used for further process. We think that this study combines the bio-based product in an interesting way through Hot Lithography achieving promising result to develop new green composites.

CRediT authorship contribution statement

sangermano marco: Writing – review & editing, Resources. **Wolff Raffael:** Data curation. **Pezzana Lorenzo:** Methodology, Investigation, Formal analysis. **Liska Robert:** Writing – review & editing. **Stampfl Jürgen:** Resources.

Declaration of Competing Interest

The authors declare that they have no known competing financial interests or personal relationships that could have appeared to influence the work reported in this paper.

Data availability

No data was used for the research described in the article.

Appendix A. Supporting information

Supplementary data associated with this article can be found in the online version at doi:10.1016/j.addma.2023.103929.

References

[1] T.T. Wohlers, W.A. (Firm), I. Campbell, O. Diegel, R. Huff, J. Kowen, N. Mostow, W.A.. (Firm) Staff, Wohlers Report 2021: 3D Printing and Additive Manufacturing Global State of the Industry, Wohlers Associates, Incorporated, 2021. https://books.google.at/books?id=vGJszgEACAAJ.
[2] S.C. Ligon, R. Liska, J. Stampfl, M. Gurr, R. Mülhaupt, Polymers for 3D Printing and Customized Additive Manufacturing, Chem. Rev. 117 (2017) 10212–10290, https://doi.org/10.1021/acs.chemrev.7b00074.
[3] F.P.W. Melchels, J. Feijen, D.W. Grijpma, A review on stereolithography and its applications in biomedical engineering, Biomaterials 31 (2010) 6121–6130, https://doi.org/10.1016/j.biomaterials.2010.04.050.
[4] M. Shahbazi, H. Jäger, Current status in the utilization of biobased polymers for 3D printing process: a systematic review of the materials, processes, and challenges, ACS Appl. Bio Mater. 4 (2021) 325–369, https://doi.org/10.1021/acsabm.0c01379.
[5] B. Lu, H. Lan, H. Liu, Additive manufacturing frontier: 3D printing electronics, Opto-Electron. Adv. 1 (2018) 170004.
[6] R. Wolff, P. Knaack, K. Seidler, C. Gorsche, T. Koch, J. Stampfl, R. Liska, Additive manufacturing of high-performance polycyanurates via photo-induced catalytic poly-trimerization, J. Mater. Chem. A. 11 (2023) 10545–10550, https://doi.org/10.1039/D3TA01264F.

[7] E. Sacco, S.K. Moon, Additive manufacturing for space: status and promises, Int. J. Adv. Manuf. Technol. 105 (2019) 4123–4146, https://doi.org/10.1007/s00170-019-03786-z.

[8] S.A. Kumar, A. Pathania, A. Shrivastava, V. Rajkumar, P. Raghupatruni, Applications of Additive Manufacturing Techniques in Aerospace Industry, : Nanotechnol. Addit. Manuf. (2023) 561–578, https://doi.org/10.1002/9783527835478.ch19.

[9] A. Bagheri, J. Jin, Photopolymerization in 3D printing, ACS Appl. Polym. Mater. 1 (2019) 593–611.

[10] E. MacDonald, R. Salas, D. Espalin, M. Perez, E. Aguilera, D. Muse, R.B. Wicker, 3D printing for the rapid prototyping of structural electronics, IEEE Access 2 (2014) 234–242, https://doi.org/10.1109/ACCESS.2014.2311810.

[11] M. Pagac, J. Hajnys, Q.-P. Ma, L. Jancar, J. Jansa, P. Stefek, J. Mesicek, A Review of Vat Photopolymerization Technology: Materials, Applications, Challenges, and Future Trends of 3D Printing, Polym 13 (2021), https://doi.org/10.3390/polym13040598.

[12] B. Steyrer, B. Busetti, G. Harakály, R. Liska, J. Stampfl, Hot Lithography vs. room temperature DLP 3D-printing of a dimethacrylate, Addit. Manuf. 21 (2018) 209–214, https://doi.org/10.1016/j.addma.2018.03.013.

[13] G. Peer, P. Dorfinger, T. Koch, J. Stampfl, C. Gorsche, R. Liska, Photopolymerization of Cyclopolymerizable Monomers and Their Application in Hot Lithography, Macromolecules 51 (2018) 9344–9353, https://doi.org/10.1021/acs.macromol.8b01991.

[14] C. Gorsche, R. Harikrishna, S. Baudis, P. Knaack, B. Husar, J. Laeuger, H. Hoffmann, R. Liska, Real Time-NIR/MIR-Photorheology: A Versatile Tool for the in Situ Characterization of Photopolymerization Reactions, Anal. Chem. 89 (2017) 4958–4968, https://doi.org/10.1021/acs.analchem.7b00272.

[15] N. Klikovits, L. Sinawehl, P. Knaack, T. Koch, J. Stampfl, C. Gorsche, R. Liska, UV-Induced Cationic Ring-Opening Polymerization of 2-Oxazolines for Hot Lithography, ACS Macro Lett. 9 (2020) 546–551, https://doi.org/10.1021/acsmacrolett.0c00055.

[16] Y. Mete, K. Seidler, C. Gorsche, T. Koch, P. Knaack, R. Liska, Cationic photopolymerization of cyclic esters at elevated temperatures and their application in hot lithography, Polym. Int. 71 (2022) 1062–1071, https://doi.org/10.1002/pi.6430.

[17] C. Dall'Argine, A. Hochwallner, N. Klikovits, R. Liska, J. Stampf, M. Sangermano, Hot-Lithography SLA-3D Printing of Epoxy Resin, Macromol. Mater. Eng. 305 (2020) 1–6, https://doi.org/10.1002/mame.202000325.

[18] L. Pierau, C. Elian, J. Akimoto, Y. Ito, S. Caillol, D.L. Versace, Bio-sourced monomers and cationic photopolymerization–The green combination towards eco-friendly and non-toxic materials, Prog. Polym. Sci. 127 (2022) 101517, https://doi.org/10.1016/j.progpolymsci.2022.101517.

[19] X. Chen, S. Chen, Z. Xu, J. Zhang, M. Miao, D. Zhang, Degradable and recyclable bio-based thermoset epoxy resins, Green. Chem. 22 (2020) 4187–4198, https://doi.org/10.1039/d0gc01250e.

[20] J.A. Poveda-Giraldo, J.C. Solarte-Toro, C.A. Cardona Alzate, The potential use of lignin as a platform product in biorefineries: A review, Renew. Sustain. Energy Rev. 138 (2021) 110688, https://doi.org/10.1016/j.rser.2020.110688.

[21] P. Chavan, A.K. Singh, G. Kaur, Recent progress in the utilization of industrial waste and by-products of citrus fruits: A review, J. Food Process Eng. 41 (2018) 1–10, https://doi.org/10.1111/jfpe.12895.

[22] L. Pezzana, E. Malmström, M. Johansson, M. Sangermano, UV-curable bio-based polymers derived from industrial pulp and paper processes, Polym 13 (2021), https://doi.org/10.3390/polym13091530.

[23] A.C. Weems, K.R. Delle Chiaie, J.C. Worch, C.J. Stubbs, A.P. Dove, Terpene- and terpenoid-based polymeric resins for stereolithography 3D printing, Polym. Chem. 10 (2019) 5959–5966, https://doi.org/10.1039/c9py00950g.

[24] A. Gandini, T.M. Lacerda, From monomers to polymers from renewable resources: Recent advances, Prog. Polym. Sci. 48 (2015) 1–39, https://doi.org/10.1016/j.progpolymsci.2014.11.002.

[25] V. Baret, A. Gandini, E. Rousset, Photodimerization of heteroarylene-vinylenes, J. Photochem. Photobiol. A Chem. 103 (1997) 169–175, https://doi.org/10.1016/S1010-6030(96)04525-X.

[26] A. Gandini, T. M. Lacerda, Furan Polymers: State of the Art and Perspectives, Macromol. Mater. Eng. 307 (2022) 2100902, https://doi.org/10.1002/mame.202100902.

[27] L. Pezzana, G. Melilli, N. Guigo, N. Sbirrazzuoli, M. Sangermano, Photopolymerization of furan-based monomers: Exploiting UV-light for a new age of green polymers, React. Funct. Polym. 185 (2023) 105540, https://doi.org/10.1016/j.reactfunctpolym.2023.105540.

[28] C. Aouf, C. Le Guernevé, S. Caillol, H. Fulcrand, Study of the O-glycidylation of natural phenolic compounds. The relationship between the phenolic structure and the reaction mechanism, Tetrahedron 69 (2013) 1345–1353, https://doi.org/10.1016/j.tet.2012.11.079.

[29] S. Ma, T. Li, X. Liu, J. Zhu, Research progress on bio-based thermosetting resins, Polym. Int. 65 (2016) 164–173, https://doi.org/10.1002/pi.5027.

[30] L. Pezzana, M. Sangermano, Fully biobased UV-cured thiol-ene coatings, Prog. Org, Coatings 157 (2021) 106295.

[31] C. Li, J. Dai, X. Liu, Y. Jiang, S. Ma, J. Zhu, Green Synthesis of a Bio-Based Epoxy Curing Agent from Isosorbide in Aqueous Condition and Shape Memory Properties Investigation of the Cured Resin, Macromol. Chem. Phys. 217 (2016) 1439–1447, https://doi.org/10.1002/macp.201600055.

[32] L. Fertier, M. Ibert, C. Buffe, R. Saint-Loup, C. Joly-Duhamel, J.-J. Robin, O. Giani, New biosourced UV curable coatings based on isosorbide, Prog. Org. Coat. 99 (2016) 393–399, https://doi.org/10.1016/j.porgcoat.2016.07.001.

[33] C. Noè, L. Iannucci, S. Malburet, A. Graillot, M. Sangermano, S. Grassini, New UV-Curable Anticorrosion Coatings from Vegetable Oils, Macromol. Mater. Eng. 306 (2021) 1–11, https://doi.org/10.1002/mame.202100029.

[34] C. Noè, S. Malburet, A. Bouvet-Marchand, A. Graillot, C. Loubat, M. Sangermano, Cationic photopolymerization of bio-renewable epoxidized monomers, Prog. Org. Coat. 133 (2019) 131–138, https://doi.org/10.1016/j.porgcoat.2019.03.054.

[35] C. Noè, S. Malburet, E. Milani, A. Bouvet-Marchand, A. Graillot, M. Sangermano, Cationic UV-curing of epoxidized cardanol derivatives, Polym. Int. 69 (2020) 668–674, https://doi.org/10.1002/pi.6031.

[36] L. Pezzana, R. Wolff, G. Melilli, N. Guigo, N. Sbirrazzuoli, J. Stampfl, R. Liska, M. Sangermano, Hot-lithography 3D printing of biobased epoxy resins, Polym. (Guildf.) 254 (2022) 125097, https://doi.org/10.1016/j.polymer.2022.125097.

[37] A. Gandini, Polymers from renewable resources: A challenge for the future of macromolecular materials, Macromolecules 41 (2008) 9491–9504, https://doi.org/10.1021/ma801735u.

[38] A. Gandini, The irruption of polymers from renewable resources on the scene of macromolecular science and technology, Green. Chem. 13 (2011) 1061–1083, https://doi.org/10.1039/C0GC00789G.

[39] S. Miao, P. Wang, Z. Su, S. Zhang, Vegetable-oil-based polymers as future polymeric biomaterials, Acta Biomater. 10 (2014) 1692–1704, https://doi.org/10.1016/j.actbio.2013.08.040.

[40] R. Mustapha, A.R. Rahmat, R. Abdul Majid, S.N.H. Mustapha, Vegetable oil-based epoxy resins and their composites with bio-based hardener: A short review, Polym. Technol. Mater. 58 (2019) 1311–1326.

[41] C. Vazquez-Martel, L. Becker, W.V. Liebig, P. Elsner, E. Blasco, Vegetable Oils as Sustainable Inks for Additive Manufacturing: A Comparative Study, ACS Sustain. Chem. Eng. 9 (2021) 16840–16848, https://doi.org/10.1021/acssuschemeng.1c06784.

[42] A. Barkane, O. Platnieks, M. Jurinovs, S. Gaidukovs, Thermal stability of UV-cured vegetable oil epoxidized acrylate-based polymer system for 3D printing application, Polym. Degrad. Stab. 181 (2020) 109347, https://doi.org/10.1016/j.polymdegradstab.2020.109347.

[43] A. Barkane, O. Platnieks, M. Jurinovs, S. Kasetaite, J. Ostrauskaite, S. Gaidukovs, Y. Habibi, UV-Light Curing of 3D Printing Inks from Vegetable Oils for Stereolithography, Polym. (Basel) 13 (2021), https://doi.org/10.3390/polym13081195.

[44] A. Barkane, M. Jurinovs, S. Briede, O. Platnieks, P. Onufrijevs, Z. Zelca, S. Gaidukovs, Biobased Resin for Sustainable Stereolithography: 3D Printed Vegetable Oil Acrylate Reinforced with Ultra-Low Content of Nanocellulose for Fossil Resin Substitution, 3D Print. Addit. Manuf. (2022), https://doi.org/10.1089/3dp.2021.0294.

[45] Z. Liu, D.A. Knetzer, J. Wang, F. Chu, C. Lu, P.D. Calvert, 3D printing acrylated epoxidized soybean oil reinforced with functionalized cellulose by UV curing, J. Appl. Polym. Sci. 139 (2022), https://doi.org/10.1002/app.51561.

[46] C. Noè, A. Cosola, C. Tonda-Turo, R. Sesana, C. Delprete, A. Chiappone, M. Hakkarainen, M. Sangermano, DLP-printable fully biobased soybean oil composites, Polym. (Guildf.) (2022).

[47] M. Jurinovs, A. Barkane, O. Platnieks, S. Beluns, L. Grase, R. Dieden, M. Staropoli, D.F. Schmidt, S. Gaidukovs, Vat Photopolymerization of Nanocellulose-Reinforced Vegetable Oil-Based Resins: Synergy in Morphology and Functionalization, ACS Appl. Polym. Mater. 5 (2023) 3104–3118, https://doi.org/10.1021/acsapm.3c00245.

[48] N. Vidakis, M. Petousis, N. Michailidis, J.D. Kechagias, N. Mountakis, A. Argyros, O. Boura, S. Grammatikos, High-performance medical-grade resin radically reinforced with cellulose nanofibers for 3D printing, J. Mech. Behav. Biomed. Mater. 134 (2022) 105408, https://doi.org/10.1016/j.jmbbm.2022.105408.

[49] M. Maturi, C. Spanu, N. Fernández-Delgado, S.I. Molina, M. Comes Franchini, E. Locatelli, A. Sanz de León, Fatty acid – functionalized cellulose nanocomposites for vat photopolymerization, Addit. Manuf. 61 (2023) 103342, https://doi.org/10.1016/j.addma.2022.103342.

[50] J.L. Speier, The preparation and properties of (hydroxyorgano)-silanes and related compounds, J. Am. Chem. Soc. 74 (1952) 1003–1010.

[51] S. Członka, A. Strąkowska, A. Kairytė, Effect of walnut shells and silanized walnut shells on the mechanical and thermal properties of rigid polyurethane foams, Polym. Test. 87 (2020) 106534.

[52] R. Coatings, C. Society, U.S.P. Convention, Standard Test Method for Epoxy Content of Epoxy Resins, Acs. khuj (6789) 4–7. https://doi.org/10.1520/D1652–11R19.2.

[53] D. Lascano, A. Lerma-Canto, V. Fombuena, R. Balart, N. Montanes, L. Quiles-Carrillo, Kinetic Analysis of the Curing Process of Biobased Epoxy Resin from Epoxidized Linseed Oil by Dynamic Differential Scanning Calorimetry, Polym. (Basel) 13 (2021), https://doi.org/10.3390/polym13081279.

[54] G. Mashouf Roudsari, A.K. Mohanty, M. Misra, Study of the curing kinetics of epoxy resins with biobased hardener and epoxidized soybean oil, ACS Sustain. Chem. Eng. 2 (2014) 2111–2116, https://doi.org/10.1021/sc500176z.

[55] R. Wolff, K. Ehrmann, P. Knaack, K. Seidler, C. Gorsche, T. Koch, J. Stampfl, R. Liska, Photo-chemically induced polycondensation of a pure phenolic resin for additive manufacturing, Polym. Chem. (2022), https://doi.org/10.1039/d1py01665b.

[56] J.V. Crivello, Effect of temperature on the cationic photopolymerization of epoxides, J. Macromol. Sci. Part A Pure Appl. Chem. 45 (2008) 591–598, https://doi.org/10.1080/10601320802168710.

[57] J.V. Crivello, B. Falk, M.R. Zonca, Photoinduced Cationic Ring-Opening Frontal Polymerizations of Oxetanes and Oxiranes, J. Polym. Sci. Part A Polym. Chem. 42 (2004) 1630–1646, https://doi.org/10.1002/pola.20012.

[58] B. Falk, M.R. Zonca, J.V. Crivello, Photoactivated cationic frontal polymerization, Macromol. Symp. 226 (2005) 97–108, https://doi.org/10.1002/masy.200550810.
[59] J.V. Crivello, S. Liu, Photoinitiated cationic polymerization of epoxy alcohol monomers, J. Polym. Sci. Part A Polym. Chem. 38 (2000) 389–401, https://doi.org/10.1002/(SICI)1099-0518(20000201)38:3<389::AID-POLA1>3.0.CO;2-G.
[60] M. Sharif, B. Pourabbas, M. Sangermano, F. Sadeghi Moghadam, M. Mohammadi, I. Roppolo, A. Fazli, The effect of graphene oxide on UV curing kinetics and properties of SU8 nanocomposites, Polym. Int. 66 (2017) 405–417, https://doi.org/10.1002/pi.5271.
[61] R. Bongiovanni, E.A. Turcato, A. Di Gianni, S. Ronchetti, Epoxy coatings containing clays and organoclays: Effect of the filler and its water content on the UV-curing process, Prog. Org. Coat. 62 (2008) 336–343, https://doi.org/10.1016/j.porgcoat.2008.01.014.
[62] C. Esposito Corcione, G. Malucelli, M. Frigione, A. Maffezzoli, UV-curable epoxy systems containing hyperbranched polymers: Kinetics investigation by photo-DSC and real-time FT-IR experiments, Polym. Test. 28 (2009) 157–164, https://doi.org/10.1016/j.polymertesting.2008.11.002.
[63] S. Malburet, C. Di Mauro, C. Noè, A. Mija, M. Sangermano, A. Graillot, Sustainable access to fully biobased epoxidized vegetable oil thermoset materials prepared by thermal or UV-cationic processes, RSC Adv. 10 (2020) 41954–41966, https://doi.org/10.1039/D0RA07682A.
[64] D.S. Branciforti, S. Lazzaroni, C. Milanese, M. Castiglioni, F. Auricchio, D. Pasini, D. Dondi, Visible light 3D printing with epoxidized vegetable oils, Addit. Manuf. 25 (2019) 317–324, https://doi.org/10.1016/j.addma.2018.11.020.
[65] R.P. Rosa, G. Rosace, R. Arrigo, G. Malucelli, Preparation and Characterization of 3D-Printed Biobased Composites Containing Micro-or Nanocrystalline Cellulose, Polym. (Basel) 14 (2022), https://doi.org/10.3390/polym14091886.
[66] A. Barkane, M. Jurinovs, O. Starkova, L. Grase, D.F. Schmidt, S. Gaidukovs, Enhancing Stiffness, Toughness, and Creep in a 3D-Printed Bio-Based Photopolymer Using Ultra-Low Contents of Nanofibrillated Cellulose, J. Compos. Sci. 7 (2023), https://doi.org/10.3390/jcs7100435.
[67] B. Wang, J. Zhou, Z. Wang, S. Mu, R. Wu, Z. Wang, Cellulose nanocrystal/plant oil polymer composites with hydrophobicity, humidity-sensitivity, and high wet strength, Carbohydr. Polym. 231 (2020) 115739, https://doi.org/10.1016/j.carbpol.2019.115739.
[68] A. Etale, A.J. Onyianta, S.R. Turner, S.J. Eichhorn, Cellulose: A Review of Water Interactions, Applications in Composites, and Water Treatment, Chem. Rev. 123 (2023) 2016–2048, https://doi.org/10.1021/acs.chemrev.2c00477.
[69] N. Ding, X. Song, Y. Jiang, B. Luo, X. Zeng, Y. Sun, X. Tang, T. Lei, L. Lin, Cooking with active oxygen and solid alkali facilitates lignin degradation in bamboo pretreatment, Sustain. Energy Fuels. 2 (2018) 2206–2214, https://doi.org/10.1039/C8SE00181B.
[70] N. Ding, H. Liu, Y. Sun, X. Tang, T. Lei, F. Xu, X. Zeng, L. Lin, Lignin degradation in cooking with active oxygen and solid Alkali process: A mechanism study, J. Clean. Prod. 278 (2021) 123984, https://doi.org/10.1016/j.jclepro.2020.123984.
[71] G. Yang, B.J. Rohde, M.L. Robertson, Hydrolytic degradation and thermal properties of epoxy resins derived from soybean oil, Green. Mater. 1 (2013) 125–134, https://doi.org/10.1680/gmat.12.00023.